

# Non-resonant viscous theory for the stability of a fluid-filled gyroscope

JEAN-PIERRE LAMBELIN<sup>1</sup>, FRANÇOIS NADAL<sup>1†</sup>,  
ROMAIN LAGRANGE<sup>2</sup> AND ARTHUR SARTHOU<sup>3</sup>

<sup>1</sup>Commissariat à l'Énergie Atomique, CESTA, 33114 Le Barp, France

<sup>2</sup>IRPHE, CNRS, Université Aix Marseille I & II, 49 rue Joliot-Curie, 13013 Marseille, France

<sup>3</sup>Université Bordeaux I, TREFLE-ENSCPB, UMR CNRS 8508, 16 avenue Pey-Berland,  
33607 Pessac Cedex, France

(Received 24 July 2008; revised 26 June 2009; accepted 30 June 2009; first published online  
16 October 2009)

In the case of a gyroscope including a cylindrical fluid-filled cavity, the classic Poinot's coning motion can become unstable. For certain values of the solid inertia ratio, the coning angle opens under the effect of the hydrodynamic torque. The coupled dynamics of such a non-solid system is ruled by four dimensionless numbers: the small viscous parameter  $\epsilon = Re^{-1/2}$  (where  $Re$  denotes the Reynolds number), the fluid–solid inertia ratio  $\kappa$  which quantifies the proportion of liquid relative to the total mass of the gyroscope, the solid inertia ratio  $\sigma$  and the aspect ratio  $h$  of the cylindrical cavity. The calculation of the hydrodynamic torque on the solid part of the gyroscope requires the preliminary evaluation of the possibly resonant flow inside the cavity. The hydrodynamic scaling used to derive such a flow essentially depends on the relative values of  $\kappa$  and  $\epsilon$ . For small values of the ratio  $\sqrt{\kappa}/\epsilon$  (compared to 1), Gans derived an expression of the growth rate of the coning angle. The principles of Gans' approach (Gans, *AIAA J.*, vol. 22, 1984, pp. 1465–1471) are briefly recalled but the details of the whole calculation are not given. At the opposite limit, that is for large values of  $\sqrt{\kappa}/\epsilon$ , the dominating flow is given by a linear inviscid theory. In order to take account of viscous effects, we propose a direct method involving an exhaustive calculation of the flow at order  $\epsilon$ . We show that the deviations from Stewartson's inviscid theory (Stewartson, *J. Fluid Mech.*, vol. 5, 1958, p. 577) do not originate from the viscous shear at the walls but rather from the bulk pressure at order  $\epsilon$  related to the Ekman suction. Physical contents of Wedemeyer's heuristic theory (Wedemeyer, BRL Report N 1325, 1966) are analysed in the view of our analytical results. The latter are tested numerically in a large range of parameters. Complete Navier–Stokes (NS) equations are solved in the cavity. The hydrodynamic torque obtained by numerical integration of the stress is used as a forcing term in the coupled fluid–solid equations. Numerical results and analytical predictions show a fairly good quantitative agreement.

---

## 1. Introduction

The behaviour of an isolated precessing tank is very dependent on the hydrodynamics of the fluid contained and approaches by energy dissipation evaluation (Garg, Furunoto & Vanyo 1986; Vanyo 1993), although very useful, can be insufficient. An accurate prediction of a possible destabilization of the coupled fluid-structure

† Email address for correspondence: Francois.Nadal@cea.fr

system implies a good understanding of the flow forced by the precessional motion of the container.

Initial theoretical work on rotating fluids can be attributed to Sir W. Thomson (Thomson 1880), who suggested that the linear inviscid flow of a disturbed rotating fluid could be written as a sum of so-called *Kelvin modes*. Using Lord Kelvin's approach, Greenhill (1880) calculated the inviscid flow in a rotating ellipsoidal cavity. As shown later by Kudlick (1966) and Greenspan (1968) for sufficiently high Reynolds numbers, viscous effects can be taken in account as corrections to Kelvin's inviscid approach. Experiments performed later (Fultz 1959; McEwan 1970; Kerswell & Barenghi 1995; Kobine 1995, 1996; Meunier *et al.* 2008) confirmed not only the values of the resonant eigen frequencies but also the times of viscous decay predicted by these linear theories. A theoretical expression of the viscously saturated amplitude at the resonance was established by Gans (1970). Meunier *et al.* (2008) confirmed Gans' prediction and gave a more complete expression for the amplitude of the resonant mode, taking in account both viscous and nonlinear terms in Navier–Stokes (NS) equations. However, further experimental work performed at sufficiently high Reynolds numbers (McEwan 1970; Thomson 1970; Manasseh 1992, 1994, 1996; Mahalov 1993) showed a systematic destabilization of the resonant flow into a fine-scale turbulent flow. This so-called *resonant collapse*, probably resulting from a triad mechanism (Lagrange 2008), was explored by Kerswell (1999). In the present work, we do not take into account nonlinear effects such as triadic coupling scenario of destabilization, since only very small coning angles are considered.

Pioneering theoretical work on the stability of a fluid-filled gyroscope was performed by Milne (1940), who applied Greenhill's inviscid solution for an ellipsoidal cavity to a completely liquid-filled spinning projectile, and exhibited a stability criterion in the form of a diagram (the so-called Milne's graph). Two decades later, Stewartson (1958) extended Milne's approach (Milne 1940) to the case of a partially or completely filled cylindrical cavity (Stewartson's theory was also based on the assumption that the inside liquid had zero viscosity). Milne–Stewartson's theory revealed the existence of unstable ranges of solid inertia ratio, for which the coning motion of the gyroscope forces a Kelvin mode close to one of its resonances. However, the discrepancies between these theories and the experiments performed by Ward (1959) were confirmed by further experimental data presented by Karpov (1962, 1965), Scott & D'Amico (1973) and D'Amico (1977, 1981). Indeed, the observed resonant frequency of the fluid-filled gyroscope was slightly (but systematically) shifted compared to the inviscid resonant frequency predicted by Stewartson (by *resonant frequency*, we mean here the frequency at which the growth rate of the coning angle is maximum). Besides, the growth rate of the coning angle was not strictly zero outside the range of unstable solid inertia ratios predicted by Stewartson.

Wedemeyer (1965, 1966) gave the first interpretation of these observations, invoking a change in the effective aspect ratio of the cylindrical cavity due to the thickness of the viscous boundary layers. Wedemeyer's theory, which is valid at high Reynolds numbers, is based on the following equivalence: the viscous system of aspect ratio  $H/R_c$  ( $H$  and  $R_c$  denote the height and radius of the cylindrical cavity) behaves as an inviscid system of aspect ratio  $(H - \delta H)/(R_c - \delta R_c)$ , where  $\delta H$  and  $\delta R_c$  are the thicknesses of the viscous boundary layers on the top and lateral walls of the cylinder, respectively. At sufficiently high Reynolds numbers, the thicknesses of both boundary layers are proportional to  $\epsilon$ . Consequently, since the value of the inviscid resonant frequency only depends on the aspect ratio, Wedemeyer's approach leads to a shift proportional to  $\epsilon$  at leading order. In principle, Wedemeyer's work, as an extension

of Stewartson's inviscid theory, does not hold in a close vicinity of any hydrodynamic resonance.

Gans (1984) derived an expression of the growth rate of the coning angle which is valid close to the resonance by applying the saturated viscous solution proposed by Gans (1970) himself to the dynamics of a near-resonant fluid-filled gyroscope. Instead of considering the main contribution of the flow as inviscid, the author calculates the viscously saturated amplitude of the main resonant Kelvin mode. This amplitude, which is  $O(\epsilon^{-1})$ , is determined by a solvability condition for the problem at the next order.

The main objective of the paper is to extend in a rigorous way Stewartson's inviscid theory to the case of a viscous fluid. Unlike Wedemeyer, whose method is heuristic, we adopt a perturbative approach that allows for an exhaustive calculation of the different viscous contributions to the total hydrodynamic torque. This method guarantees that all the contributions of same order are taken into account. The second objective is to perform an identification of Wedemeyer's physical ingredients, which are not clear due to the intuitive nature of the work.

The paper is organized as follows. In §2, we first present a reminder of Stewartson's approach (Stewartson 1958). We propose a simple criterion which defines the limit of validity of the theory presented in §3. The main steps of the theory are given in the body of the article, while the tedious details of the calculations are gathered in the appendices. Precisions concerning the regime of applicability of Wedemeyer's theory are given at the end of §3. In §4, theoretical results are tested for a large range of physical parameters (Reynolds number  $Re$ , fluid–solid inertia ratio  $\kappa$ ) by means of numerical simulations. Discrepancies between the numerical results and the present theory are discussed at the end of the section.

## 2. Presentation of the problem

### 2.1. Definition of the frame of reference – kinematics

A cylindrical cavity full of fluid (viscosity  $\mu$ , density  $\rho$  and kinematic viscosity  $\nu = \mu/\rho$ ) is included in an axisymmetrical solid rigid body. Both solid and fluid parts of the gyroscope have the same axis of symmetry  $\hat{\mathbf{k}}$ . The centre of gravity of the whole system is supposed to be located at the centroid of the cylindrical cavity and we assume the mass of fluid is relatively small compared to that of the solid.  $\mathcal{R}_0$  denotes the inertial reference frame.

Two sets of non-inertial frames are then introduced, depending on whether we are interested in the hydrodynamics of the contained liquid or in the fluid-structure coupled dynamics. Unitary vectors related to a given reference frame are referred to as  $\mathbf{x}$ ,  $\mathbf{y}$  and  $\mathbf{z}$  with the appropriate subscript. The first set of reference frames ( $\mathcal{R}_\psi$ ,  $\mathcal{R}_\theta$ ,  $\mathcal{R}_\phi$ ), suitable for the hydrodynamics, corresponds to the classic Euler's coordinates  $(\psi, \theta, \phi)$ , as shown in figure 1(a). In the reference frame of the cylinder  $\mathcal{R}_\phi$ , the position of any point is defined by its polar coordinates  $(R, \varphi, Z)$ . Integrality of the theoretical analysis for hydrodynamics is achieved in  $\mathcal{R}_\phi$ . In the remainder of the text, spin angular velocity  $\dot{\phi}$  and precessional velocity  $\dot{\psi}$  are referred to as  $\Omega_1$  and  $\Omega_2$ , respectively.  $\boldsymbol{\Omega}$  is the time-dependent rotation vector of the whole system.

The second set ( $\mathcal{R}_\alpha$ ,  $\mathcal{R}_\beta$ ), suitable for the study of the coupled fluid-structure dynamics, corresponds to the Cardan's coordinates  $(\alpha, \beta)$  as depicted in figure 1(b). Actually,  $\mathcal{R}_\alpha$  and  $\mathcal{R}_\beta$  are the natural reference frames for classic experimental gyroscopes.

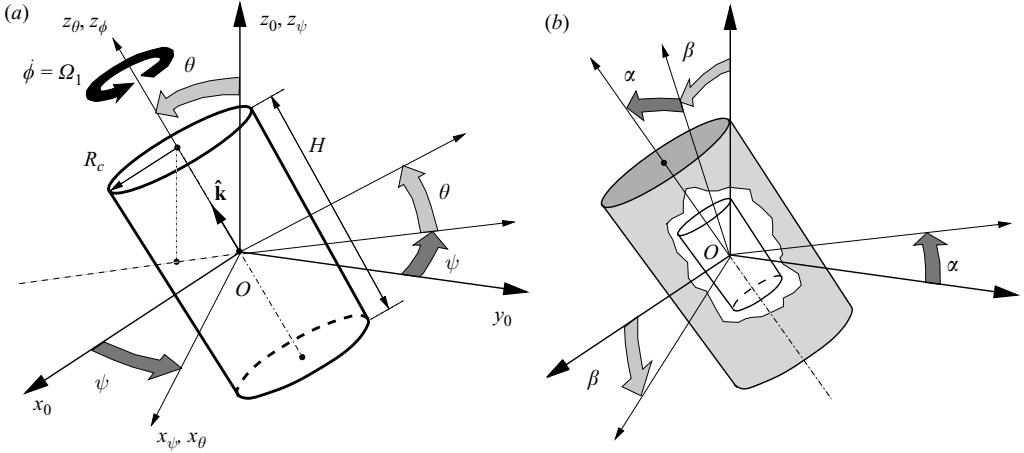


FIGURE 1. Definition of the frames of reference. (a) Euler's angles suitable for hydrodynamics. (b) Cardan's angles suitable for coupled fluid-structure dynamics.

## 2.2. Formulation of hydrodynamics

The NS equations, written in the non-Galilean frame of reference  $\mathcal{R}_\phi$  take on the following form

$$\frac{\partial \mathbf{U}}{\partial T} + (\mathbf{U} \cdot \nabla) \mathbf{U} + 2 \boldsymbol{\Omega} \times \mathbf{U} + \frac{d\boldsymbol{\Omega}}{dT} \times \mathbf{R} + \boldsymbol{\Omega} \times (\boldsymbol{\Omega} \times \mathbf{R}) = -\frac{1}{\rho} \nabla P + \nu \Delta \mathbf{U} \quad (2.1a)$$

and

$$\nabla \cdot \mathbf{U} = 0, \quad (2.1b)$$

with the boundary condition  $\mathbf{U} = \mathbf{0}$  at the walls. In (2.1a),  $\mathbf{R}$ ,  $\mathbf{U}$  and  $P$  refer to the radius vector, fluid velocity and pressure, respectively. The last three inertial terms of the left member are the Coriolis acceleration, the acceleration due to the non-stationarity of  $\boldsymbol{\Omega}$  and to centrifugal acceleration. As we consider the case  $O' = O$ , the term coming from the acceleration of the centre of gravity vanishes (otherwise, it could be incorporated in the pressure gradient). To specify the relative position of  $\mathcal{R}_\phi$  and  $\mathcal{R}_\theta$  at  $T = 0$ , we write

$$\boldsymbol{\Omega} = \Omega [\hat{\mathbf{k}} + \varepsilon \boldsymbol{\eta}(T)], \quad (2.2)$$

with  $\Omega = \boldsymbol{\Omega} \cdot \hat{\mathbf{k}} = \Omega_1 + \Omega_2 \cos \theta$ ,  $\varepsilon = \Omega_2 \sin \theta / \Omega$  and  $\boldsymbol{\eta}(T) = \cos(\Omega_1 T) \mathbf{x}_\phi - \sin(\Omega_1 T) \mathbf{y}_\phi$ . Equation (2.1a) can be made dimensionless by choosing  $\varepsilon \Omega R_c$ ,  $\Omega^{-1}$  and  $R_c$  as typical scales for velocity, time and distance, respectively. Using lowercase letters for dimensionless quantities and neglecting the nonlinear terms (proportional to  $\varepsilon^2$ ), we obtain the linear dimensionless form of (2.1a)

$$\frac{\partial \mathbf{u}}{\partial t} + 2 \hat{\mathbf{k}} \times \mathbf{u} + \nabla p = -2\omega r \cos(\omega t + \varphi) \hat{\mathbf{k}} + \varepsilon^2 \Delta \mathbf{u}, \quad (2.3)$$

where  $\varepsilon = (\Omega R_c^2 / \nu)^{-1/2} = Re^{-1/2}$  is the small viscous parameter and  $\omega = \Omega_1 / \Omega$ . The dimensionless pressure, which includes every potential terms, is

$$p = \frac{P}{\rho \varepsilon \Omega^2 R_c^2} - \frac{1}{2} \frac{r^2}{\varepsilon} + (1 - \omega) r z \cos(\omega t + \varphi). \quad (2.4)$$

Further comments must be made on the hypothesis of linearization of (2.1a). For the nonlinear effects to be negligible in comparison with the viscous ones, the ratio  $\varepsilon^2 / \varepsilon$

must be greater than 1. This condition can be rewritten  $\theta < |1 - \omega|^{-1} Re^{-1}$ . As the forcing frequency and the Reynolds number are known in each case, the limit angle beyond which the nonlinear effects intervene is fixed (at least in order of magnitude).

In the remainder of the paper,  $(u, v, w)$  are the dimensionless cylindrical components of  $\mathbf{u}$  in the reference frame  $\mathcal{R}_\phi$  and, for the sake of concision in the notations,  $\mathbf{v} = (\mathbf{u}, p)$  designates the velocity–pressure field.

Let us give now the expression of the complex solution to the inviscid form ( $\epsilon = 0$ ) of (2.3). The inviscid flow  $\mathbf{v}^{(0)}$  in a forced precessing cylinder has been calculated by several authors (cf. Greenspan 1968 for example). It can be sought in the form of a particular solution  $\mathbf{v}_{part.}$  completed by an infinite sum of Kelvin modes

$$\mathbf{v}^{(0)} = \mathbf{v}_{part.} + \sum_{i=1}^{\infty} a_i^{(0)} \mathbf{v}_i^{(0)} e^{i(\omega t + \varphi)}. \quad (2.5)$$

In the previous expression,  $\mathbf{v}_i^{(0)} e^{i(\omega t + \varphi)}$  is the Kelvin mode of axial wavenumber  $k_i^{(0)}$ , radial wavenumber  $\delta_i^{(0)}$  and frequency  $\omega$  with

$$\mathbf{v}_i^{(0)} = \begin{pmatrix} i \frac{\omega r \delta_i^{(0)} J_1'(\delta_i^{(0)} r) + 2J_1(\delta_i^{(0)} r)}{r(\omega^2 - 4)} \sin(k_i^{(0)} z) \\ - \frac{2r \delta_i^{(0)} J_1'(\delta_i^{(0)} r) + \omega J_1(\delta_i^{(0)} r)}{r(\omega^2 - 4)} \sin(k_i^{(0)} z) \\ i \frac{k_i^{(0)}}{\omega} J_1(\delta_i^{(0)} r) \cos(k_i^{(0)} z) \\ J_1(\delta_i^{(0)} r) \sin(k_i^{(0)} z) \end{pmatrix}, \quad (2.6)$$

and the particular solution is

$$\mathbf{v}_{part.} = (0, 0, 2ire^{i(\omega t + \varphi)}, 0). \quad (2.7)$$

In the following,  $u_i^{(0)}, v_i^{(0)}, w_i^{(0)}$  and  $p_i^{(0)}$  denote the four components of  $\mathbf{v}_i^{(0)}$ . The amplitude  $a_i^{(0)}$  of each Kelvin mode is given by

$$a_i^{(0)} = \frac{4\omega^2}{(\omega - 2)(k_i^{(0)2} + 1)k_i^{(0)} J_1(\delta_i^{(0)}) \cos(k_i^{(0)} h)}, \quad (2.8)$$

where  $h = H/2R_c$ . The radial wavenumber  $\delta_i^{(0)}$  satisfies the Kelvin's relation

$$\omega \delta_i^{(0)} J_1'(\delta_i^{(0)}) + 2J_1(\delta_i^{(0)}) = 0, \quad \text{with } |\omega| < 2 \quad (2.9)$$

and the axial wavenumber  $k_i^{(0)}$  the constitutive relation

$$\delta_i^{(0)2} = \frac{4 - \omega^2}{\omega^2} k_i^{(0)2}. \quad (2.10)$$

The first four Kelvin branches corresponding to the dispersion relation (2.9) and (2.10) are plotted in figure 2(a). As shown by the expression (2.8), the amplitude  $a_i^{(0)}$  of each Kelvin mode diverges (see figure 2b) for an infinity of wavenumbers  $k_n = \pi(2n - 1)/2h$  (with  $n$  a non-zero integer) for which the quantity  $\cos(k_i^{(0)} h) = 0$ . Thus, in the range  $[-2, 2]$ , a double infinity of resonant frequencies  $\omega_{i,n}$  is obtained by considering on each branch the frequencies for which  $k_i^{(0)} = k_n$ . Note that the expression (2.8) does not hold any longer for  $\omega$  in a close vicinity of any  $\omega_{i,n}$ , where Gans' expression of viscously saturated amplitude proved to be more relevant.

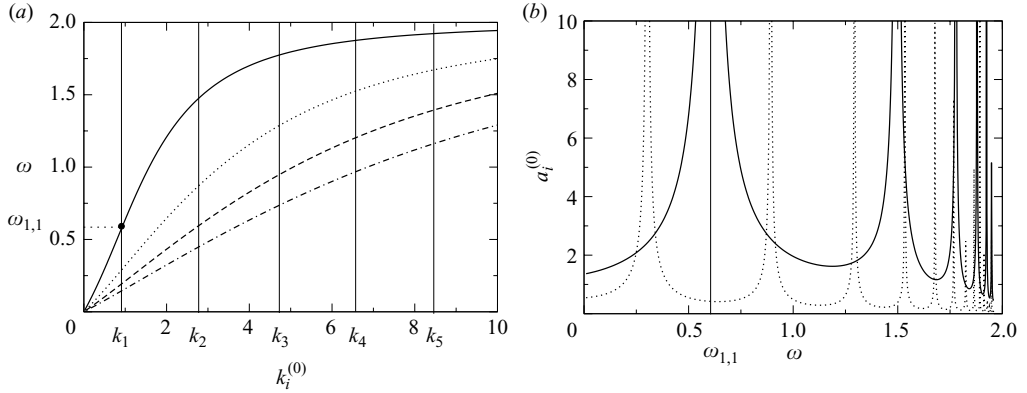


FIGURE 2. Inviscid theory for a precessing cylinder full of fluid ( $R_c = 0.33$  m,  $H = 0.1$  m). (a) Kelvin's relation of dispersion. Only the first four branches are plotted:  $i = 1$  (solid),  $i = 2$  (dotted),  $i = 3$  (dashed) and  $i = 4$  (dot-dashed). (b) Amplitude of the first two Kelvin modes given by the inviscid theory:  $i = 1$  (solid) and  $i = 2$  (dotted). Numerical simulations presented in §4 are performed around the first resonance of the first mode  $\omega_{1,1} = 0.605$ .

### 2.3. Coupled dynamics formulation and Milne–Stewartson theory

Since the only torque acting on the solid part of the gyroscope comes from the hydrodynamic stress, one can write

$$\frac{d\mathbf{J}\boldsymbol{\Omega}}{dt} = \mathbf{M}, \quad (2.11)$$

where  $\mathbf{J}$  is the inertial tensor (which is diagonal in  $\mathcal{R}_\phi$ ), and  $\mathbf{M}$  the hydrodynamic torque resulting from the integration of hydrodynamic constraints on the cavity walls. In (2.11), the time derivative is considered in  $\mathcal{R}_0$ . Projecting (2.11) on the  $x_\alpha$ - and  $y_\alpha$ -axis leads to the system

$$A \ddot{\alpha} + C \Omega \dot{\beta} = M_{x_\alpha}, \quad (2.12a)$$

$$A \ddot{\beta} - C \Omega \dot{\alpha} = M_{y_\alpha}, \quad (2.12b)$$

where  $A$  and  $C$  respectively denote the transverse and lengthwise inertia momenta of the solid part of the gyroscope ( $\mathbf{J} = [A, A, C]$  in  $\mathcal{R}_\phi$ ). Equation (2.12) is equivalent to the more convenient form

$$A \ddot{\zeta} - iC\Omega \dot{\zeta} = M_{y_\alpha} - iM_{x_\alpha}, \quad (2.13)$$

where  $\zeta = \beta - i\alpha$  is the complex angular variable. In the linearized equations (2.12) and (2.13), quadratic terms involving  $\alpha$ ,  $\beta$  and their time derivatives are neglected owing to the assumption  $\alpha, \beta \ll 1$ , which is required for consistency with the earlier assumption of small coning angles. For an empty cavity ( $\mathbf{M} = \mathbf{0}$ ), the solid describes the classic precessional Poincaré's motion for which the axis  $\hat{\mathbf{k}}$  generates a cone of a fixed half-angle  $\theta$  at the angular velocity  $\Omega_2 = (C/A)\Omega$ . In this case  $\zeta = \theta \exp(i\Omega_2 T)$ ,  $\Omega_2$  being a real number. In the general case of a fluid-filled cavity,  $\zeta$  is to be sought in the same form, but with  $\Omega_2$  in the complex domain. The characteristic time of aperture of the coning angle then equals  $[\text{Im}(\Omega_2)]^{-1}$ .

Following Stewartson (1958), we first consider in  $\mathbf{M}$  the only contribution  $\mathbf{M}^{(0)}$  of the inviscid flow (2.5).  $\mathbf{M}^{(0)}$ , which results from the integration of  $p^{(0)}$  over the cavity walls, can be written in the reference frame  $\mathcal{R}_\alpha$  as a function of  $\omega$  and the

dimensionless precession frequency  $s = \Omega_2/\Omega$ . We obtain

$$\mathbf{M}^{(0)} = \rho \varepsilon \Omega^2 R_c^5 \left[ m^{(0)} + 2\pi h (1 - \omega) \left( \frac{h^2}{3} - \frac{1}{4} \right) \right] e^{ist} [\mathbf{y}_\alpha + i \mathbf{x}_\alpha], \quad (2.14)$$

where

$$m^{(0)} = 2\pi \sum_{i=1}^{\infty} a_i^{(0)} \left[ \frac{J_2(\delta_i^{(0)})}{\delta_i^{(0)}} \sin(k_i^{(0)}h) - \frac{J_1(\delta_i^{(0)})}{k_i^{(0)2}} [\sin(k_i^{(0)}h) - (k_i^{(0)}h) \cos(k_i^{(0)}h)] \right] \quad (2.15)$$

is  $O(1)$ . Let us now consider a unique resonant frequency  $\omega_0$  among the double infinity of  $\omega_{i,n}$ . We assume  $\omega_0$  is far enough from any other main hydrodynamic resonance. The relevance of this assumption is partially ensured by the viscous criterion of viability established by Gans (1970). Gans' inequality  $\delta_i^{(0)} < Re^{1/7}$  stipulates that for a given Reynolds number, the Kelvin modes of high radial wavenumbers cannot be forced due to the viscous effects. For sufficiently low Reynolds numbers, this condition is likely to drastically reduce the density of resonances in the vicinity of  $\omega_0$ . Considering the values of  $Re$  used in the present paper, the resonance  $\omega_0 = \omega_{1,1}$  (which is examined further) will be regarded as isolated, but such a verification must be performed in each particular case.

So, the main diverging term is therefore kept in the Laurent's expansion of the involved Kelvin mode, namely,

$$m^{(0)} \simeq \frac{D^{(0)}}{\omega_0 - \omega}. \quad (2.16)$$

The expression of  $D^{(0)}$  is given in Appendix A. Using the previous expression of  $m^{(0)}$  and the general form  $\zeta = \theta \exp(ist)$  in (2.13), we can rewrite the latter as a polynomial equation of variable  $s$

$$-s + \sigma = \kappa \frac{D^{(0)}}{s - s_0}, \quad (2.17)$$

where

$$\sigma = C/A', \quad \kappa = \rho R_c^5/A', \quad s_0 = 1 - \omega_0 \quad \text{and} \quad A' = A + 2\pi \left( \frac{h^2}{3} - \frac{1}{4} \right). \quad (2.18)$$

To derive (2.17), it is recalled that the case of small coning angles is considered, for which the approximations  $s \simeq 1 - \omega$  and  $\varepsilon \simeq \theta s$  are valid. Moreover, the assumption of quasi-staticity of the coning angle  $\theta$  is supposed to be satisfied, namely,  $\dot{\theta} \ll \theta \Omega_2$  at any time. Actually, in the coupled situation, the part of the term  $d\Omega/dT$  in (2.1a) coming from the variation of the nutation angle  $\theta$  (recall that  $\dot{\theta} = 0$  in the forced regime), must be negligible compared to the one coming from the precession. This condition, which can be rewritten  $\text{Im}(s)/\text{Re}(s) \ll 1$ , defines the limit of use of the flow (2.5) in a situation in which  $\theta$  is free to evolve. In other words, (2.17) is valid for complex values of  $s$ , as long as  $\text{Im}(s) \ll \text{Re}(s)$ .

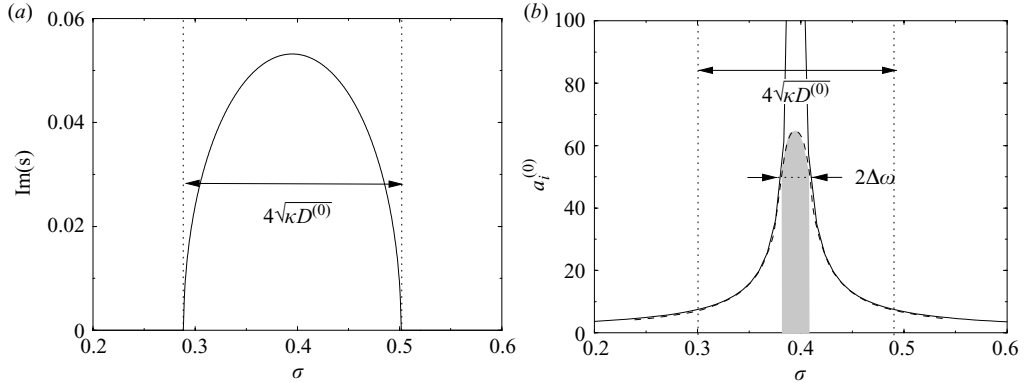


FIGURE 3. Criterion of validity for corrected Stewartson's theories. In these plots, we used  $\kappa = 0.003$ ,  $D^{(0)} = 0.9493$  and  $\epsilon = 0.009$ . (a) Imaginary part of  $s$  as a function of the inertia ratio  $\sigma$ . (b) inviscid (solid) and viscous (dashed) amplitudes of the Kelvin mode. The criterion of applicability (2.21) characterizes the width of the inviscid unstable domain (Stewartson's theory for the coupled problem) compared to the width of the hydrodynamic viscous domain.

The physically acceptable solution to (2.17) depends on the range in which the inertia ratio  $\sigma$  lies

$$s = \frac{1}{2} [(\sigma + s_0) - i[4\kappa D^{(0)} - (\sigma - s_0)^2]^{1/2}] \quad \text{for } |\sigma - s_0| < 2\sqrt{\kappa D^{(0)}}, \quad (2.19a)$$

$$s = \frac{1}{2} [(\sigma + s_0) - [(\sigma - s_0)^2 - 4\kappa D^{(0)}]^{1/2}] \quad \text{for } \sigma < s_0 - 2\sqrt{\kappa D^{(0)}}, \quad (2.19b)$$

$$s = \frac{1}{2} [(\sigma + s_0) + [(\sigma - s_0)^2 - 4\kappa D^{(0)}]^{1/2}] \quad \text{for } \sigma > s_0 + 2\sqrt{\kappa D^{(0)}}. \quad (2.19c)$$

All the previous results have been established by Milne (1940) and Stewartson (1958), for the case of spheroidal and cylindrical cavities, respectively. The reduced growth rate  $\text{Im}(s)$  is plotted as a function of the inertia ratio  $\sigma$  in figure 3(a). As shown in the plot, inertial effects at  $Re = \infty$  make the fluid-filled gyroscope unstable in a range of width  $4\sqrt{\kappa D^{(0)}}$  around  $s_0$ . The maximum rate of divergence is  $\sqrt{\kappa D^{(0)}}$ .

#### 2.4. Criterion of applicability for corrected Stewartson's theories

As the main objective of the paper is to extend rigorously Stewartson's inviscid theory to the case of a viscous liquid, we have to figure out in which case (i.e. for which set of physical parameters) such an approach can be adopted (rather than Gans' approach).

First, the point is to evaluate the width  $\Delta\omega$  of the Gans' 'window', that is to say the range of forcing frequency in which the amplitude of the main flow is saturated by the viscous effects. Based on Meunier's modified Gans' theory (Meunier 2008), one can show that the inviscid solution (2.5) is not valid anymore, as soon as the forcing frequency lies in a domain of width

$$\Delta\omega \sim \epsilon \bar{a}^{(0)} f^{-1} \max[|\mu|, \nu] \quad (2.20)$$

around the resonance. Details of the derivation of the previous expression are given in Appendix B. In (2.20),  $\mu$ ,  $\nu$  and  $f$  are the surface and volume viscous parameters and the forcing parameter derived by Meunier *et al.* (2008), the expressions of which are also reminded in Appendix B. The expression of  $\bar{a}^{(0)}$  is given in Appendix A (the subscript 'i' has been removed since there is no ambiguity about the resonance).



Thus, for a forcing frequency of width  $\Delta\omega$  around  $\omega_0$ , the inviscid solution is diverging, which makes any corrective approach irrelevant. It therefore appears natural to expect any Stewartson's corrected approach to be of interest provided the inviscid unstable domain (of width  $\sim \sqrt{\kappa D^{(0)}}$ ) is wider than the range of viscous saturation  $\Delta\omega$ , namely (see figure 3),

$$\sqrt{\kappa} > \epsilon \frac{\bar{a}^{(0)}}{2\sqrt{D^{(0)}}f} \max[|\mu|, \epsilon\nu]. \quad (2.21)$$

In (2.21) constitutes a (sufficient) criterion of applicability of the theory presented in the next section. In other words, (2.21) tells us if there is or not a domain where Stewartson's corrected theories are relevant. However, (2.21) does not tell us in which domain of forcing frequency these theories can be used. Actually, for the theory presented in the next section to apply, the forcing frequency  $\omega$  must stand outside the Gans' window, namely,

$$|\omega - \omega_0| > \Delta\omega. \quad (2.22)$$

The previous inequality can be rewritten using the inertia parameter  $\sigma = C/A'$  and considering that  $\sigma \simeq \text{Re}(s) \simeq 1 - \omega$ ,

$$|1 - \sigma - \omega_0| > \Delta\omega. \quad (2.23)$$

This previous criterion of validity characterizes the *corrected inertial regime*, that is to say the domain of forcing frequency in which the Stewartson's corrected theories apply.

### 3. Treatment of viscous effects in the corrected inertial regime

The pressure torque calculated from the inviscid solution becomes destabilizing in a domain of frequency of width  $4\sqrt{\kappa D^{(0)}}$  around  $\omega_0$ . Nonetheless, experiments performed by Karpov (1962, 1965) with real liquids clearly show a non-zero growth rate outside the inviscid unstable domain. Unlike Wedemeyer, we present in the next section a direct calculation of the viscous corrections responsible for instance of such a broadening of the unstable region. The connection with Wedemeyer's theoretical results is made afterwards.

In the inertial coupling limit, the global velocity–pressure field is sought in the form of a double  $\epsilon$ -expansion  $\mathbf{v} = \mathbf{v}_{out} + \mathbf{v}_{in}$  with

$$\mathbf{v}_{out} = \mathbf{v}^{(0)} + \epsilon \mathbf{v}^{(1)} + O(\epsilon^2) \text{ in the bulk,} \quad (3.1a)$$

$$\mathbf{v}_{in} = \tilde{\mathbf{v}}^{(0)} + \epsilon \tilde{\mathbf{v}}^{(1)} + O(\epsilon^2) \text{ inside the boundary layer.} \quad (3.1b)$$

In addition, the condition  $\mathbf{v}_{in} = \mathbf{0}$  outside the boundary layer is required.

#### 3.1. Viscous and pressure torques

Before going further, the relative orders of magnitude of the torques must be discussed. Quantities with dimension are therefore considered to the end of this paragraph. A hydrodynamic torque corresponds to each term of the previous expansions. Thus,  $\mathbf{M}^{(0)}$ , which intervenes in Stewartson's theory, results from the integration of the pressure at leading order in bulk over the cavity walls. In the following,  $\widetilde{\mathbf{M}}^{(0)}$  notes the torque due to the viscous shear at leading order,  $\mathbf{M}^{(1)}$  and  $\widetilde{\mathbf{M}}^{(1)}$  designate the torques resulting from integration of the pressures at order  $\epsilon$  outside and inside the boundary layer, respectively. Note that the torque resulting from the pressure at leading order in the boundary layer is always zero (see Appendix C).

As shown by (2.14),  $\mathbf{M}^{(0)}$  is of the same order of magnitude as the scaling factor  $\rho\epsilon\Omega^2 R_c^5$  whereas  $\widetilde{\mathbf{M}}^{(0)}$  proves to be one order greater in  $\epsilon$ , that is  $\widetilde{\mathbf{M}}^{(0)} \sim \epsilon\mathbf{M}^{(0)}$ . Indeed, as the viscous constraint at leading order is of order  $\mu\epsilon^{-1}\epsilon\Omega$ , the order of magnitude of the corresponding torque is  $\mu\epsilon^{-1}\epsilon\Omega R_c^3 = \rho\epsilon\epsilon\Omega^2 R_c^5$ . Generally, it can be shown that the shear torque  $\widetilde{\mathbf{M}}^{(q)}$  calculated at a given order  $\epsilon^q$  in velocity is of the order  $\epsilon\mathbf{M}^{(q)}$ , where  $\mathbf{M}^{(q)}$  is the torque calculated at the same order  $\epsilon^q$  in pressure. Consequently, taking account only of the torque  $\widetilde{\mathbf{M}}^{(0)}$  for the coupling as Murphy (1982) is altogether questionable, the pressure torques  $\mathbf{M}^{(1)}$  and  $\widetilde{\mathbf{M}}^{(1)}$  being of the same order. This also means that the pressures at order  $\epsilon$  inside and outside the boundary layer must be derived explicitly. As shown in §3.4, the main contribution of the viscous destabilization comes from the torque  $\mathbf{M}^{(1)}$ .

### 3.2. Flows at leading order and order $\epsilon$

In principle, a direct integration of the NS equations could lead to the expression of the flow at order  $\epsilon$  in bulk. However, to avoid such a tedious pathway, it can be seen that both flows at leading order and at order  $\epsilon$  satisfy the same inviscid NS equations in bulk (if we forget the forcing term). This suggests seeking  $\mathbf{v}^{(1)}$  by expanding the radial and lengthwise wavenumbers  $\delta_i = \delta_i^{(0)} + \epsilon\delta_i^{(1)}$  and  $k_i = k_i^{(0)} + \epsilon k_i^{(1)}$  in a global field  $\mathbf{v}_{out}^{(0)}$  of the same shape as the inviscid solution  $\mathbf{v}^{(0)}$ .

As we will see further, this is not sufficient to satisfy the boundary conditions at order  $\epsilon$  on top and bottom walls. The solution is to complete the  $\epsilon$ -expanded flow by an additional flow ‘parallel’ to  $\mathbf{v}^{(0)}$  (same shape, same wavenumbers  $\delta_i^{(0)}$  and  $k_i^{(0)}$ , but different amplitudes  $a_i^+$  of the Kelvin modes). Note that doing this is equivalent to expanding the amplitude in the flow  $\mathbf{v}_{out}$ . This extra flow does not disturb the boundary condition on the lateral wall but permits the normal velocity at order  $\epsilon$  to equal the Ekman pumping on the top and bottom wall.

Consequently, the flow in the bulk  $\mathbf{v}_{out}$  can be written as

$$\mathbf{v}_{out} = \mathbf{v}^{(0)} + \epsilon \sum_{i=1}^{\infty} \left[ a_i^+ \mathbf{v}_i^{(0)} + a_i^{(0)} \left( \delta_i^{(1)} \frac{\partial \mathbf{v}_i^{(0)}}{\partial \delta_i} + k_i^{(1)} \frac{\partial \mathbf{v}_i^{(0)}}{\partial k_i} \right) \right] e^{i(\omega t + \varphi)} + O(\epsilon^2), \quad (3.2)$$

where all the partial derivatives are considered at  $(\delta_i^{(0)}, k_i^{(0)})$ . The amplitudes  $a_i^{(0)}$  are still unknown at this stage.

The shape of the velocity–pressure field is fixed by the previous equation in which the unknown quantities  $\delta_i^{(1)}$  and  $k_i^{(1)}$  must be determined in order to satisfy the boundary conditions at order  $\epsilon$ . In practice, the normal component of the velocity at order  $\epsilon$  in bulk must equal the Ekman pumping at the wall, which results from the non-homogeneity of the corrective viscous flow in the boundary layer (see e.g. Waleffe 1989).

#### 3.2.1. Leading order

We shall not revert to the resolution of the inviscid flow  $\mathbf{v}^{(0)}$  given in §2.2. At this stage, the amplitudes  $a_i^{(0)}$  are fixed by the inviscid boundary condition of tangential velocity at the walls. The classical derivation of the corrective viscous flow  $\widetilde{\mathbf{v}}^{(0)}$  is given in Appendix C.

#### 3.2.2. Order $\epsilon$

The expressions of the normal Ekman components  $u_i^+ e^{i(\omega t + \varphi)}$  (on the lateral wall) and  $w_i^+ e^{i(\omega t + \varphi)}$  (on the top and bottom walls) arising from the  $i$ th Kelvin mode are also given in Appendix C. The boundary condition at order  $\epsilon$  applied to the flow

given by (3.2) for a unique Kelvin mode

$$a_i^{(0)} \delta_i^{(1)} \frac{\partial u_i^{(0)}}{\partial \delta_i} = u_i^\perp \quad \text{at } r = 1 \quad (3.3)$$

leads to the expression of  $\delta_i^{(1)}$  (see again Appendix C for details):

$$\delta_i^{(1)} = \frac{1 - i}{\sqrt{2\omega}} \delta_i^{(0)}. \quad (3.4)$$

Once the expression of  $\delta_i^{(1)}$  has been established, the correction to the lengthwise wavenumber  $k_i^{(1)}$  is fixed by the constituting relation (2.10) (which is also valid at order  $\epsilon$ ) and can not be freely chosen to satisfy the boundary conditions at order  $\epsilon$  on top and bottom walls. Indeed, as the global field  $\mathbf{v}_{out}$  is a solution of the inviscid NS equation, the quantities  $\delta_i^{(0)} + \epsilon \delta_i^{(1)}$  and  $k_i^{(0)} + \epsilon k_i^{(1)}$  are connected by the constituting relation

$$[\delta_i^{(0)} + \epsilon \delta_i^{(1)}]^2 = \frac{4 - \omega^2}{\omega^2} [k_i^{(0)} + \epsilon k_i^{(1)}]^2, \quad (3.5)$$

which involves

$$\delta_i^{(1)2} = \frac{4 - \omega^2}{\omega^2} k_i^{(1)2}. \quad (3.6)$$

Due to this lack of available ‘degree of freedom’, the introduction of the extra flows  $a_i^+ \mathbf{v}_i^{(0)}$  turns to be indispensable in order to properly compensate the Ekman pumping on top and bottom walls.

So, at the top and bottom walls, we have

$$a_i^{(0)} \left[ \delta_i^{(1)} \frac{\partial w_i^{(0)}}{\partial \delta_i} + k_i^{(1)} \frac{\partial w_i^{(0)}}{\partial k_i} \right] + a_i^+ w_i^{(0)} = w_i^\perp \quad \text{for } z = \pm h. \quad (3.7)$$

The calculation of the amplitudes  $a_i^+$  of the Kelvin modes in the additional flow is exhaustively presented in Appendix D. Thus, the boundary conditions at every wall are satisfied, and we finally get the pressure related to the flow in the bulk at order  $\epsilon$ :

$$p^{(1)} = \sum_{i=1}^{\infty} a_i^{(0)} \left[ \delta_i^{(1)} \frac{\partial p_i^{(0)}}{\partial \delta_i} + k_i^{(1)} \frac{\partial p_i^{(0)}}{\partial k_i} \right] e^{i(\omega t + \varphi)} + \sum_{i=1}^{\infty} a_i^+ p_i^{(0)} e^{i(\omega t + \varphi)}. \quad (3.8)$$

The pressure  $\tilde{p}^{(1)}$  in the boundary layer can be directly obtained by integrating the systems of equations (C 1a) and (C 1b) given in Appendix C. The expression of  $\tilde{p}^{(1)}$  is given in Appendix E.

### 3.3. Coupled dynamics

The new equation of coupling takes the following form:

$$-s + \sigma = \kappa [m^{(0)} + \epsilon(\tilde{m}^{(0)} + m^{(1)} + \tilde{m}^{(1)})]. \quad (3.9)$$

The expressions of the complex torques  $m^{(1)}$ ,  $\tilde{m}^{(1)}$  and  $\tilde{m}^{(0)}$  are collated in Appendix E. As specified above, these torques result from the integration of  $p^{(1)}$ ,  $\tilde{p}^{(1)}$  and the viscous stress related to  $\tilde{\mathbf{u}}^{(0)}$ , respectively.

Following again Stewartson (inviscid coupling), each torque can be replaced by its Laurent’s expansion. In this case, expansions are truncated after the last diverging term. For instance, the torques  $\tilde{m}^{(0)}$  and  $\tilde{m}^{(1)}$ , which only contain poles of order 1, can

$(i, n)$	$\omega_{i,n}$	$\tilde{D}_R^{(0)}$	$\tilde{D}_I^{(0)}$	$\tilde{D}_R^{(1)}$	$\tilde{D}_I^{(1)}$	$C_R^{(1)}$	$C_I^{(1)}$	$D_R^{(1)}$	$D_I^{(1)}$
(1, 1)	0.6047	-1.6326	1.3488	5.0075	5.0075	0.2676	1.2304	-4.7988	-1.6445
(1, 2)	1.4961	-0.7388	1.3982	0.0616	0.0616	0.01	-0.1489	1.0049	3.4896
(2, 1)	0.3026	-0.1572	0.1166	1.4323	1.4323	0.0368	0.1481	-1.6148	-1.1687
(2, 2)	0.8922	-0.0497	0.1944	0.0227	0.0277	0.0005	0.0031	0.1867	0.5526

TABLE 1. Coefficients of Laurent's expansion of the torques at order  $\epsilon$  evaluated at the first two resonances modes of the first two Kelvin modes  $i = 1$  and  $i = 2$ , for a cylinder of aspect ratio  $h = 1.65$ .

be written as

$$\tilde{m}^{(0)} = \frac{\tilde{D}_R^{(0)}}{s - s_0} + i \frac{\tilde{D}_I^{(0)}}{s - s_0}, \quad (3.10a)$$

$$\tilde{m}^{(1)} = \frac{\tilde{D}_R^{(1)}}{s - s_0} + i \frac{\tilde{D}_I^{(1)}}{s - s_0}. \quad (3.10b)$$

Expressions of the real quantities  $\tilde{D}_R^{(0)}$ ,  $\tilde{D}_I^{(0)}$ ,  $\tilde{D}_R^{(1)}$  and  $\tilde{D}_I^{(1)}$  are collated in Appendix E. As for the torque  $m^{(1)}$ , which contains poles of order 1 and 2, it can be written in the form

$$m^{(1)} = \left[ \frac{C_R^{(1)}}{(s - s_0)^2} + \frac{D_R^{(1)}}{s - s_0} \right] + i \left[ \frac{C_I^{(1)}}{(s - s_0)^2} + \frac{D_I^{(1)}}{s - s_0} \right]. \quad (3.11)$$

Expressions of the real quantities  $C_R^{(1)}$ ,  $C_I^{(1)}$  are also given in Appendix E. Tedious expressions of the real quantities  $D_R^{(1)}$  and  $D_I^{(1)}$  are not given exhaustively in the paper, but their values for the first two resonances of the Kelvin modes  $i = 1$  and  $i = 2$  for a cylinder of aspect ratio  $h = 1.65$  are given in table 1.

At order  $\epsilon$ , (3.9) is equivalent to

$$-s + \sigma = \kappa \left[ \frac{D^{(0)} + \epsilon(D_R + iD_I)}{s - [s_0 + \epsilon(s_R + i s_I)]} \right], \quad (3.12)$$

where

$$D_R = \tilde{D}_R^{(0)} + \tilde{D}_R^{(1)} + D_R^{(1)}, \quad (3.13a)$$

$$D_I = \tilde{D}_I^{(0)} + \tilde{D}_I^{(1)} + D_I^{(1)}, \quad (3.13b)$$

$$s_R = C_R^{(1)}/D^{(0)}, \quad (3.13c)$$

$$s_I = C_I^{(1)}/D^{(0)}. \quad (3.13d)$$

### 3.4. Comparison with Wedemeyer's approach

Equation (3.12) makes the connection with Wedemeyer's theory. Indeed, Wedemeyer's characteristic equation of coupling (given for example in Whiting & Gerber 1981) is formally almost identical to (3.12) where  $D_R$  and  $D_I$  are set to zero. The difference comes from the important fact that Wedemeyer's method only takes into account the effects linked to the Ekman pumping, namely, the quantities  $s_R$  and  $s_I$  in (3.12). The viscous shear torque  $\tilde{m}^{(0)}$ , the pressure torque  $\tilde{m}^{(1)}$  are not considered in Wedemeyer's approach. Thus, if the contribution  $\epsilon(D_R + iD_I)$  is small compared to  $D^{(0)}$ , Wedemeyer's and the present theory are very close to each other, as shown in figure 4(a). They

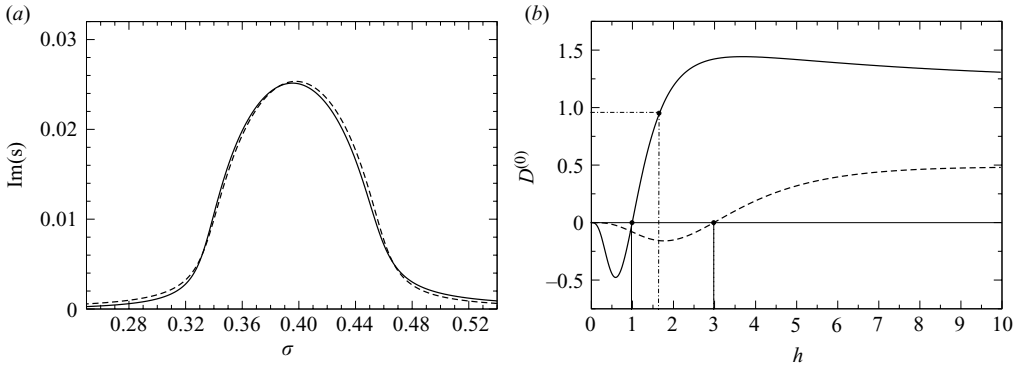


FIGURE 4. (a) Comparison of the present theory (solid line) with Wedemeyer's (dashed line) for the case II presented in the numerical section. Wedemeyer's and uncomplete present theory (obtained by taking  $D_R, D_I = 0$ ) are superimposed. (b)  $D^{(0)}$  plotted as a function of the aspect ratio  $h$  for the first (solid line) and second (dashed line) of the first Kelvin mode. For the first (resp. second) resonance,  $D^{(0)} = 0$  at  $h = 0.995$  (resp.  $h = 2.985$ ).

are completely superimposed if this quantity is neglected. When not negligible with respect to  $D^{(0)}$ , the quantity  $\epsilon(D_R + iD_I)$  is responsible for a possible asymmetry of the viscous tails.

Figure 4(b) plots the inviscid coupling coefficient  $D^{(0)}$  as a function of the aspect ratio  $h$ , for the first and second resonance of the first Kelvin mode, namely,  $\omega_{1,1}$  and  $\omega_{1,2}$ . For each resonance,  $D^{(0)}$  cancels out at a given aspect ratio ( $h = 0.995$  for the first resonance and  $h = 2.985$  for the second resonance). For such aspect ratios, the respective weights of  $D^{(0)}$  and  $\epsilon(D_R + iD_I)$  are inverted and Wedemeyer's theory is no longer suitable. Moreover, in a really close vicinity of these singular values, Laurent's expansions are not strictly valid either and must be taken one order further. Such a marginal treatment will be presented in a forthcoming communication. Note that most of the experimental studies for full cavities without an internal rod (see e.g. D'Amico 1977, 1981 and Whiting & Gerber 1981) have been performed for  $h = 1$  and  $h = 3$ .

#### 4. Numerical study

In this section, we present numerical studies performed in order to check the validity of the theoretical results reported in the previous section. The first part addresses the general features of the fluid dynamics code that is used in this study. In this part, the numerical coupling between the NS equations and the container dynamics is briefly presented. The second part deals with the numerical results. We first present results related to the hydrodynamic flow in a forced regime (for which the kinematics of the container are fixed). Numerical results for the fluid-structure coupled dynamics are detailed afterwards. Numerical studies in forced and coupled regimes are made for a cavity of fixed aspect ratio  $h = 1.65$  (height  $H = 0.33$  m and radius  $R_c = 0.1$  m).  $\Omega$  is equal to  $2\pi$  rad s $^{-1}$  and the viscosity is varied to change the Reynolds number. The lengthwise inertia  $A$  is varied to change the fluid/solid inertia ratio. We focus on the first resonance of the first mode ( $\omega_{1,1} = 0.605$ ) for which the criterion of applicability can be written in the simpler form  $\sqrt{\kappa}/\epsilon < 1$ , the rest of the right member of (2.21) being of order 1 in this case.

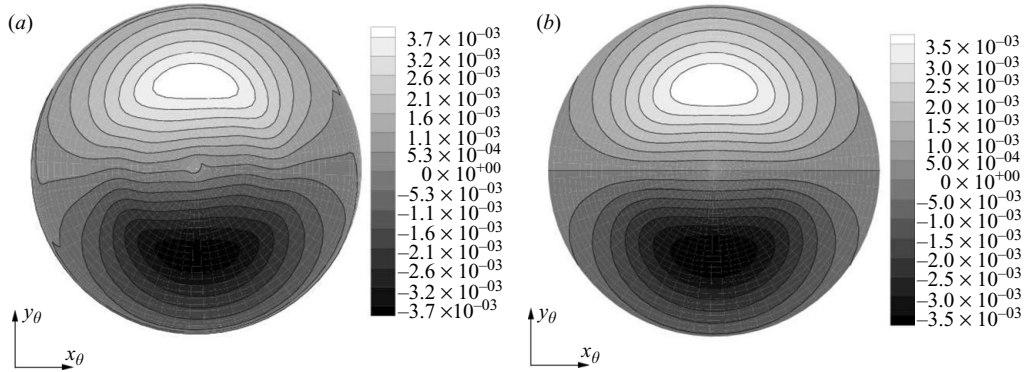


FIGURE 5. Axial component of the real velocity field on a horizontal plane located at  $z_\phi = 0$  in forced regime. Numerical values of the legend are given in  $\text{m s}^{-1}$ . The velocity field presented above corresponds to the following physical parameters:  $\Omega = 2\pi \text{ rad s}^{-1}$ ,  $\Omega_s = 3.016 \text{ rad s}^{-1}$ ,  $R = 0.1 \text{ m}$ ,  $H = 0.33 \text{ m}$ ,  $\mu = 5 \cdot 10^{-3} \text{ Pa s}$  and  $\rho = 10^3 \text{ kg m}^{-3}$ . The dimensionless frequency, the Reynolds number and the nonlinear parameter are respectively  $\omega = 0.520$ ,  $Re = 12566$  and  $\varepsilon = 1.6 \cdot 10^{-3}$ . (a) Numerical field given at time  $T = 40 \text{ s}$ . The transient stage is almost finished and lateral boundary layers are visible. (b) Analytical inviscid solution.

#### 4.1. Numerical schemes and parameters

##### 4.1.1. Hydrodynamics

NS equations (2.1a) and (2.1b) are solved by means of an augmented Lagrangian method (Fortin & Glowinski 1982; Vincent & Caltagirone 2000). Equations of motion for the fluid are discretized with a finite volumes method on fixed staggered orthogonal cylindrical grids of type Marker And Cells (Harlow & Welsh 1965). To discretize the differential form (2.1a), a second-order Euler scheme is used for the time derivative. The viscous and augmented Lagrangian terms are discretized thanks to a second-order centred scheme. The resulting linear systems are solved using a Bi-CGSTAB II iterative method (van der Vorst 1992), preconditioned under a modified and incomplete LU algorithm. A fully implicit order 2 integration scheme is used to perform time integration. A space and time convergence analysis guarantees the quality of the results. An example of numerical velocity field is presented in figure 5.

##### 4.1.2. Fluid-structure coupling

In the numerical calculations, the NS equations (2.1) are solved without any simplification. Calculation of complementary inertial terms shown in (2.1a) requires the evaluation of  $\mathbf{\Omega}$ , the Cartesian coordinates of which are  $\Omega_{x_\phi}$ ,  $\Omega_{y_\phi}$  and  $\Omega_{z_\phi}$ , in the reference frame  $\mathcal{R}_\phi$ . The rotation vector is obtained by numerical integration of the equations of motion for the solid. As the latter undergoes the hydrodynamic torque only, the evolution of its angular momentum takes the following form:

$$\dot{\Omega}_{x_\phi} = (1 - C/A) \Omega_{y_\phi} \Omega_{z_\phi} + M_{x_\phi}/A, \quad (4.1a)$$

$$\dot{\Omega}_{y_\phi} = (C/A - 1) \Omega_{z_\phi} \Omega_{x_\phi} + M_{y_\phi}/A, \quad (4.1b)$$

$$\dot{\Omega}_{z_\phi} = M_{z_\phi}/C. \quad (4.1c)$$

The coupled problem is thus ruled by (2.1) and (4.1). The coupling between the NS equations and the equations of motion of the solid is performed thanks to a time splitting method: at the current time step, the NS equations are solved using the coordinates of  $\mathbf{\Omega}$  obtained at the previous step. The hydrodynamic torque  $\mathbf{M}$

is computed by numerical integration of pressure and shear stress evaluated at the walls of the container. An Adams–Bashforth integration method of order 4 is used to perform the time integration of (4.1). This integration allows the update of  $\Omega$  and complementary acceleration terms in (2.1a) for the next step and so on.

## 4.2. Numerical results and comparison with theory

### 4.2.1. Convergence analysis and forced regime

The purpose of the studies in a forced regime is firstly to make a time and space convergence analysis, secondly to compare the amplitudes of the torque  $M^{(1)}$  with the theoretical prediction. It is in fact known that this quantity rules the process of destabilization far from the hydrodynamic resonance.

Only the space convergence analysis performed for a Reynolds number  $Re = 12566$  is presented, that is for the following fluid parameters  $\rho = 10^3 \text{ kg m}^{-3}$  and  $\mu = 0.005 \text{ Pa s}$ . The precession velocity chosen to make the analysis is  $\Omega_2 = 1.508 \text{ rad s}^{-1}$ . The corresponding dimensionless forcing frequency  $\omega = 0.520$  is located far from the resonance  $\omega_{1,1} = 0.605$ . As the main point of interest (regarding stability) is the component of the hydrodynamic torque  $M_{y\theta}$ , This quantity is used as the performance parameter in convergence analysis. Initially, the system is supposed to be in rigid rotation around the  $z_0$  axis ( $\theta = 0$ ). At  $T = 0$ , the system is instantaneously tilted towards a fixed coning angle  $\theta = 0.1$  and the flow slowly relaxes to a stationary state in the reference frame  $\mathcal{R}_\theta$ . To accurately take account of viscous effects, the boundary layers are meshed with cells of exponentially increasing size. A constant radial size is used to mesh the bulk. The characteristics of each mesh are given below in the form *number of radial divisions*  $\times$  *number of azimuthal division*  $\times$  *number of lengthwise divisions* (*number of cells in the boundary layers*). The four main grids used in the convergence study at  $Re = 12566$  are the following:  $62 \times 80 \times 132$  (8),  $50 \times 64 \times 104$  (8),  $40 \times 50 \times 82$  (6),  $32 \times 40 \times 64$  (5). When meshing, the characteristic size  $(2\nu/\Omega)^{1/2}$  is considered to be representative of the boundary layer thickness, which is not entirely relevant since there are two different characteristic lengths for the top and bottom boundary layers (see expressions (C 8)). Besides, the number of cells in the boundary layer may appear insufficient to accurately capture the corrective flow but the comparison of analytic and numerical shear stresses shows a good agreement even with only five cells in the thickness. For this sole study, a time step of  $2 \times 10^{-3} \text{ s}$  is used. Nevertheless, as the calculations are very time consuming, the stationary state has to be estimated before the extinction of the transient stage. To do so, we exploit the fact that the behaviour of the perturbed state is an exponentially damped sinus superimposed on a linear component. A convergence curve in space is presented in figure 6(a) in log-lin coordinates. The fit used to make the extrapolation to the smallest time steps is obtained by a Richardson's method.

In the time convergence analysis, the mesh  $50 \times 64 \times 104$ (8) is selected and the same set of physical parameters as in the space convergence analysis presented above are used. A first computation is performed with a rough time step of  $4 \times 10^{-3} \text{ s}$  until a nearly stationary regime in  $\mathcal{R}_\theta$  is reached. Then, a computation is made with smaller time steps until new converged values are obtained and so on. A time convergence curve is presented in figure 6(b) in lin-log coordinates. A power law is used for the extrapolation to the smallest time steps.

The conclusions related to the time and space convergence analysis are as follows: for low viscosities ( $\mu = 0.001 \text{ Pa s}$ ) a grid  $50 \times 64 \times 104$  (8) is adopted; for intermediate ( $\mu = 0.005 \text{ Pa s}$ ) and high viscosities ( $\mu = 0.01 \text{ Pa s}$ ), a coarser  $50 \times 64 \times 64$  (6) grid is

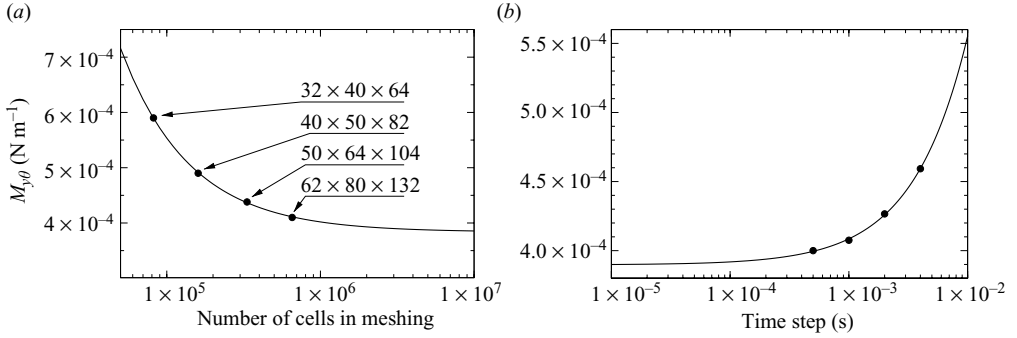


FIGURE 6. Convergence study in forced regime. (a) Space convergence:  $y_\theta$  component of the hydrodynamic torque (after stabilization) as a function of the number of cells. (b) Time convergence:  $y_\theta$  component of the hydrodynamic torque (after stabilization) as a function of the time step. Richardson's extrapolation is plotted in solid line. Numerical values are plotted in solid circles.

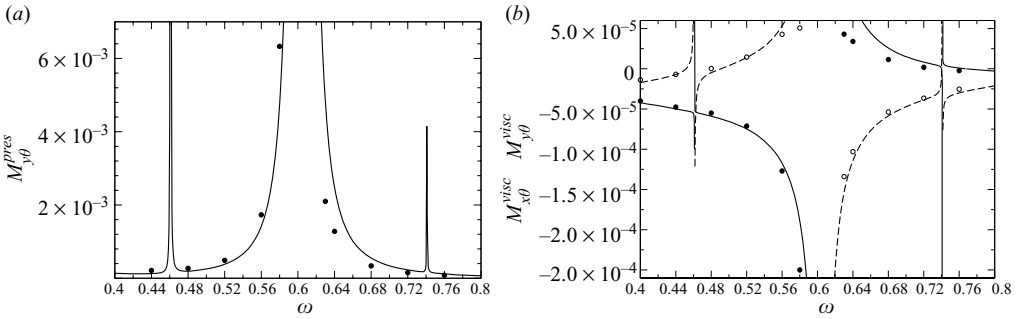


FIGURE 7. Hydrodynamic torque at order  $\epsilon$ . (a)  $y_\theta$  component of the numerical pressure torque (closed circle). Component of the theoretical torque  $\tilde{M}^{(1)} + M^{(1)}$  in the  $y_\theta$  direction is plotted in solid line. (b) Components of the numerical shear torque in the  $x_\theta$  direction (open circles) and  $y_\theta$  direction (closed circles). Corresponding theoretical components  $\tilde{M}_{x_\theta}^{(0)}$  and  $\tilde{M}_{y_\theta}^{(0)}$  are plotted in dashed and solid lines, respectively. Mesh and physical parameters are the same as in the time convergence study (see text).

used. All studies are performed with a time step of  $10^{-3}$  s, which seems to be a good compromise between precision and CPU calculation time.

The hydrodynamic torque at order  $\epsilon$  must now be addressed. Numerical experiments enable to make the distinction between pressure and shear contributions to the hydrodynamic torque. These contributions are noted  $M^{press}$  and  $M^{visc}$  respectively. The configuration chosen (meshing and physical parameters) is the same as that used for the time convergence study. The  $y_\theta$  component of the pressure torque as a function of the forcing frequency  $\omega$  is presented in figure 7(a) and both components of the shear torque are presented in figure 7(b). The forcing pulsation  $\omega$  lies in the range  $[0.4, 0.8]$  which corresponds to the domain explored in the free coupling study (§4.2.2). Agreement between numerics and theory is good for the  $x_\theta$  components of the viscous torques. In the  $y_\theta$  direction, the discrepancies for both pressure and viscous torques are greater on the right side of the resonance than on the left. This observation remains unexplained for the moment.



case	$A$ (kg m <sup>2</sup> )	$\rho$ (kg m <sup>-3</sup> )	$\mu$ (Pa s)	$Re$	$\kappa$	$\sqrt{\kappa}/\epsilon$
I	5	1500	$10^{-3}$	94247	$3.0 \cdot 10^{-3}$	16.8
II	10	1000	$5.0 \cdot 10^{-3}$	12566	$9.36 \cdot 10^{-4}$	3.40
III	100	1000	$10^{-2}$	6280	$10^{-4}$	0.79

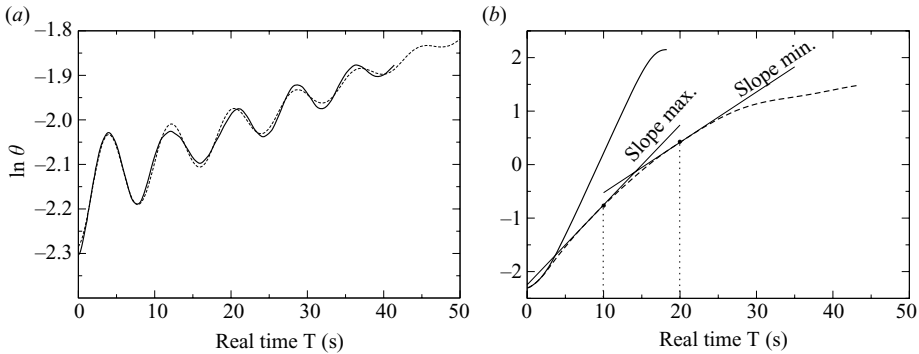
 TABLE 2. Physical parameters for each case.  $\kappa$  and  $Re$  are given for information.


FIGURE 8. Coning angle (in degrees) as a function of the real time  $T$  for case I. (a) Outside the inviscid unstable domain, initial flow relaxes through damped oscillations. The solid line corresponds to  $\sigma = 0.56$ . The fitting curve is plotted in dashed line. (b) Non-oscillating relaxation of the transient stage. For  $\sigma = 0.40$  (solid line), the evolution of the coning angle is exponential from 0.1 to about 5 and the growth rate can be evaluated without further interpretation. For  $\sigma = 0.3$  (dashed line) the evolution is not straightforwardly exponential.

#### 4.2.2. Coupled regime

Three numerical experiments (noted I, II, III) located in the corrected inertial regime are presented below. Initial conditions are the same as in the forced regime but the coning angle is free to evolve under the influence of the hydrodynamic torque. As stated in the first lines of the section, the geometry of the container and the value of  $\Omega = 2\pi$  rad s<sup>-1</sup> is the same for every case. The parameters varying from a case to another are collated in table 2. The ratio  $\sqrt{\kappa}/\epsilon$ , which is supposed to be greater than 1 for the present theory to be usable, is given in the last column. We notice that the third case stands at the edge of the domain of applicability of the present theory.

The configuration I is located in the inertial field since  $\sqrt{\kappa}/\epsilon \gg 1$ . In principle, the growth rate of the coning angle  $\text{Im}(s)$  (plotted as a function of  $\omega$  in figures 9–11) should have been obtained from numerical calculations by a simple estimation of the quantity  $d \ln[\theta(T)]/dT$  in the very first seconds of destabilization. Unfortunately, the transient stage evolves through either oscillating or non-oscillating decay, as illustrated in figure 8. Decaying oscillations correspond to situations in which the viscous effects are predominant (outside the inviscid unstable regime). In this case, estimation of the growth rate is given by assuming that the shape of  $\ln[\theta(T)]$  results from the superposition of a linear term and an exponentially damped cosine. Such an identification process provides an accurate value of the growth rate  $\text{Im}(s)$ . As we leave the viscously dominated region to enter the inviscid unstable domain, the identification of any possible linear regime proves to be difficult. The value chosen for  $\text{Im}(s)$  is given by the slope of  $\ln[\theta(T)]$  averaged over the period [ $T = 10$  s,  $T = 20$  s]. Uncertainty on the growth rate is then given by the minimum and maximum values

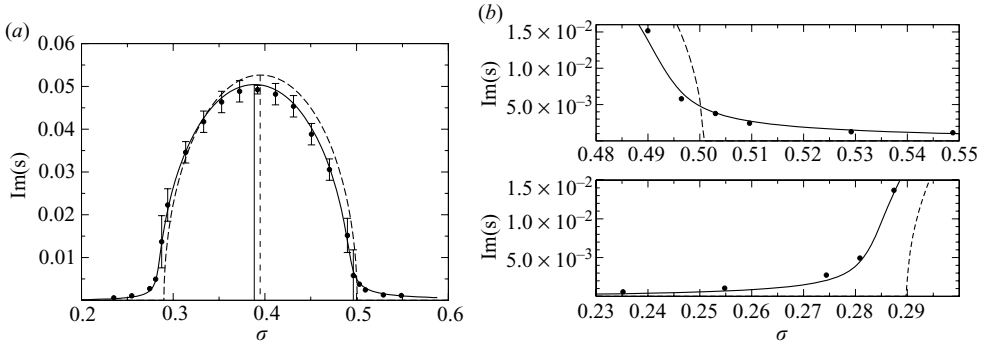


FIGURE 9. Stability curve for case I –  $\kappa = 3.0 \cdot 10^{-3}$ ,  $Re = 94247$ . (a) The present viscous theory is plotted in solid line. The dashed line corresponds to the inviscid Stewartson’s theory. The numerical results are plotted in closed circles. (b) Details of the stability curve in the domain where the viscous effects are predominant.

of the slope encountered on the same interval of time. As we move closer to the region for which  $\text{Im}(s)$  plotted as a function of  $\sigma$  is the stiffest (see figure 9a), a characteristic linear evolution can be clearly identified as shown in figure 8(b). For large coning angles ( $\theta \sim 5$ ), temporal evolution of  $\ln[\theta(T)]$  is no longer linear. This kind of behaviour, which could be the indirect signature of nonlinear phenomena such as Lagrange’s triadic instability (Lagrange 2008), has been observed in Karpov’s experimental data (Karpov 1965). In figure 9(a), the agreement between numerical and theoretical growth rates is good. The bell-shaped curve corresponding to the present theory is fairly close to the numerical data. As for the quantity  $\max[\text{Im}(s)]$ , the decay as well as the shift in  $\sigma$  observed for the numerical results (in comparison with the inviscid case) are properly calculated. Moreover, the viscous broadening observed on the numerical results outside the inviscid unstable domain of  $\sigma$  (i.e. the appearance of right and left viscous tails on the stability curve) is well predicted. However a zoom performed on the right (resp. left) viscous tail of the stability curve (figure 9b) highlights a slight but systematic underestimation (resp. overestimation) of the numerical growth rate. As shown below, this tendency is also noticeable for cases II and III.

The configuration II is also located in the inertial regime since  $\sqrt{\kappa}/\epsilon = 3.4$ . Most of the comments related to the first case are still valid. The stability curves are presented in figure 10(a). As in the previous case, the agreement between the present theory and the numerical results is satisfactory. The physically acceptable solutions of the third-order polynomial equation (3.9) are also plotted in figure 10(a). The comparison of the latter with the solutions of the second-order polynomial equation (3.12) illustrates the order of magnitude of the error made by approximating (3.9) by (3.12). As shown in figure 10(a), the third-order equation does not permit a precise determination of the shift of  $\max[\text{Im}(s)]$  since  $\epsilon$ -expansions no longer hold in the vicinity of the hydrodynamic resonance. In figure 10(a), the identification of  $\max[\text{Im}(s)]$  (and the corresponding  $\sigma$ ) becomes possible due to the ‘smoothing’ of the approximate form (3.12). This means that the value of the resonant inertial ratio (given by  $s_0 + \epsilon s_R$ ) must be considered cautiously. The situation is different in configuration I, for which both approaches give almost the same results. In figure 9(a), the corresponding curves would be superimposed. Note that the value of  $\max[\text{Im}(s)]$  is slightly underestimated by 3%–4%.

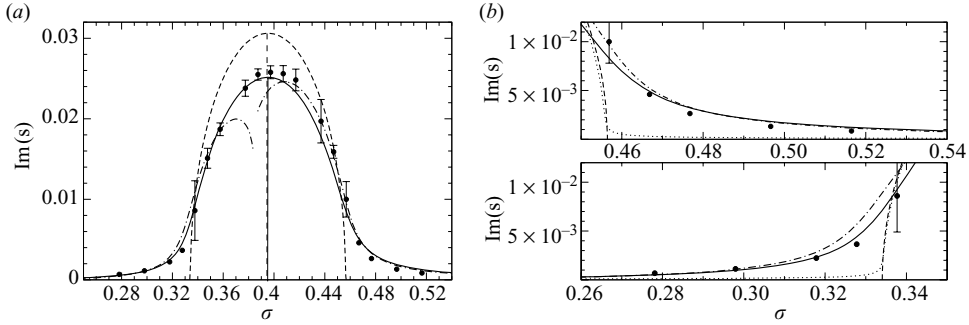


FIGURE 10. Stability curve – case II,  $\kappa = 9.36 \cdot 10^{-4}$ ,  $Re = 12566$ . (a) The viscous theory (defined in (3.12)) is plotted in solid line. The dashed line corresponds to Stewartson's inviscid theory. The dot-dashed line has been obtained by solving directly the third-order characteristic equation (3.9). The numerical results are plotted in solid circles. (b) Detailed views of the stability curve in the domains where the viscous effects are predominant. On these views the dotted curve has been obtained by selecting only the shear torque  $\tilde{m}^{(0)}$  in the derivation of the theoretical stability curve.

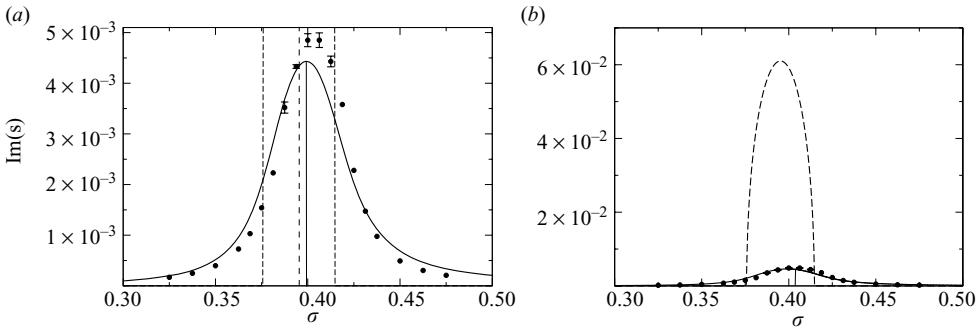


FIGURE 11. Stability curve – case III,  $\kappa = 10^{-4}$ ,  $Re = 6280$ . (a) The present viscous theory (defined in (3.12)) is plotted in solid line. The viscous effects lead to a decrease and a shift of the maximum growth rate compared to the inviscid theory (dashed line). The numerical results are plotted in closed circles. (b) Rescaled view of (a) that points out the difference between the amplitudes of inviscid and viscous theories.

In figure 10(b), the dotted curve has been obtained by selecting only the viscous shear torque  $\tilde{m}^{(0)}$  for the calculation of the stability curve. The destabilization effects obtained outside the inviscid unstable domain are one order of magnitude smaller than the effects obtained by numerical calculation. This latter observation stresses the fact that, insofar as the dimensionless torque  $m^{(1)}$  is predominant in the destabilization process, taking account only of the viscous torque  $\tilde{m}^{(0)}$  does not lead to a reasonable value of the growth rate.

The third configuration, noted III, corresponds to an intermediate situation, between the corrected inertial regime and the saturated viscous regime ( $\sqrt{\kappa}/\epsilon = 0.79$ ). The results for case III are collated in figure 11. Although this last case is located at the edge of the domain of validity of our theoretical results, the agreement between theory and numerics remains quite good. The maximum value of the growth rate is reasonably captured: the theoretical and numerical growth rates agree within 10%. However, some discrepancies are more pronounced than in cases I and II. For instance, the shift of the maximum value of the growth rate is underestimated by a factor of

2. This shortcoming is also slightly visible in figure 10(a) and can be explained as follows: on coming closer to the viscous regime ( $\sqrt{\kappa}/\epsilon \rightarrow 1$ ), the estimation of the resonance shift deteriorates, since the hydrodynamics are ruled by Gans' approach in a wider domain. In the right-hand viscous tail of the stability curve, the growth rate is overestimated of about 20%–40% in the considered range of  $\sigma$ , depending on the distance from the resonance. Once again, this tendency, although it is less obvious, can be observed for case I and II. Figure 10(b) illustrates the amplitude drop, which is about one order of magnitude, when taking account of the viscous effects.

## 5. Discussion and conclusion

The problem of a completely fluid-filled gyroscope, in the particular case of a simple cylindrical cavity, has been addressed. The whole work is valid at small coning angles, where the nonlinear effects are negligible. The Reynolds number is supposed to be high enough to allow for the boundary layer corrections. Moreover, the hydrodynamic resonance of interest is supposed to be sufficiently distant from any other resonance. This condition is satisfied as far as the Reynolds number is not too high, the threshold being fixed by Gans' criterion of viability  $\delta_i^{(0)} < Re^{1/7}$ .

Firstly, Milne–Stewartson's theory has been rewritten in a more convenient set of reference frames. By comparing the width of the inviscid unstable domain provided by Stewartson's approach to the width of the saturated viscous regime of the hydrodynamic flow studied by Gans (1970), a criterion is proposed for the present theory to be relevant. The corrected inertial regime, which corresponds to high values of  $\kappa$ , is treated theoretically and numerically. It has been shown that a direct calculation of the flows at order  $\epsilon$  (inside and outside the boundary layer) enabled the evaluation of the destabilizing pressure torques  $\widetilde{M}^{(1)}$  and  $M^{(1)}$ . In the vicinity of the resonant frequency, the latter behaves as a pole of order 2 (which is the leading term of its Laurent's expansion). It has also been shown that, when neglecting every other corrections other than the pole of order 2 in  $M^{(1)}$ , the growth rate of the coning angle obtained plotted as a function of the inertia ratio  $\sigma$  is exactly superimposed on Wedemeyer's result. This finding highlights the fact that the viscously induced destabilization principally originates from the flow at order  $\epsilon$  in bulk (namely, the flow in volume corresponding to the Ekman pumping), rather than from the viscous shear at walls. In most cases, the latter only intervenes as a correction that eventually induces a slight asymmetry on the plots of  $\text{Im}(s)$  versus  $\sigma$ . The marginal situations in which the viscous shear torque becomes predominant are not treated in the present article.

Numerical calculations were performed for a cylindrical cavity of aspect ratio  $h = 1.65$ . We focused on the first resonance of the first mode ( $i = 1, n = 1$ ) for which the criterion of regime separation can be written in the simplified form  $\sqrt{\kappa} > \epsilon$ . We explored a relatively wide range of physical parameters, since for the three numerical cases treated, the ratio  $\sqrt{\kappa}/\epsilon$  varies from 0.79 to 16.8. Use of numerical studies avoids certain experimental problems as bearing frictions and aerodynamic torques. Theoretical prediction and numerical calculations of the maximum growth rate agree to within 5%–10% depending on the case. As expected, agreement between numerics and theory deteriorates as the ratio  $\sqrt{\kappa}/\epsilon$  diminishes. The main problem concerns the restitution of the shift of  $\max[\text{Im}(s)]$  compared to the inviscid Stewartson's value. For  $\sqrt{\kappa}/\epsilon$  close to 1, this quantity is underestimated by a factor of almost two. This discrepancy is to be attributed to the irrelevance of the present theory in a very close vicinity of the resonance.

One restriction on the applicability of the present theory is that the resonance considered must not be close to the value  $\omega = 1$ . In this case, the value of the inviscid quantity  $D^{(0)}$  becomes very small and the constant term in the Laurent's expansion of  $m^{(0)}$  can no longer be omitted. In other words, for a given aspect ratio  $h$ , the resonances for which  $D^{(0)}$  is close to zero cannot be treated by the present theory and require certain refinements. The treatment of such singular resonances is still incomplected and will be presented in a forthcoming communication. Most of the experimental work has been performed in a close vicinity of singular resonances. For instance, D'Amico's experiments presented in Whiting's paper (Whiting & Gerber 1981) are made at the second resonance of the first mode, which is singular for the considered aspect ratio  $h \sim 3$ . We expect that a better understanding of such marginal situations could lead to improvements in the interpretation of several experimental results already published.

### Appendix A. Laurent's expansion of the inviscid torque

Let us consider the expression (2.15) of  $m^{(0)}$ . The leading term in Laurent's expansion of the latter is obtained by seeking the leading term in Laurent's expansion of  $a_i^{(0)}$ , the term in brackets being considered at  $\omega = \omega_0$ .

Laurent's  $\omega$ -expansion of  $a_i^{(0)}$  truncated after the first (and only) diverging term is

$$a_i^{(0)} \simeq \frac{\bar{a}_i^{(0)}}{\omega_0 - \omega}, \quad (\text{A } 1)$$

where

$$\bar{a}_i^{(0)} = \frac{4\omega_0^2}{(\omega_0 - 2)(k_i^{(0)2} + 1)k_i^{(0)}J_1(\delta_i^{(0)})h \sin(k_i^{(0)}h) dk_i^{(0)}/d\omega}. \quad (\text{A } 2)$$

In (A 2), the wavenumbers  $\delta_i^{(0)}$ ,  $k_i^{(0)}$  and the derivative  $dk_i^{(0)}/d\omega$  are considered at  $\omega = \omega_0$ , with

$$\frac{dk_i^{(0)}}{d\omega} = \frac{\omega_0}{k_i^{(0)}(4 - \omega_0^2)} \left[ \delta_i^{(0)2} + k_i^{(0)2} + \delta_i^{(0)}\omega_0 \frac{d\delta_i^{(0)}}{d\omega} \right] \quad (\text{A } 3)$$

and

$$\frac{d\delta_i^{(0)}}{d\omega} = -\frac{\delta_i^{(0)}J_1'(\delta_i^{(0)})}{(\omega_0 + 2)J_1'(\delta_i^{(0)}) + \omega_0\delta_i^{(0)}J_1''(\delta_i^{(0)})}. \quad (\text{A } 4)$$

Coming back to the Laurent's expansion of  $m^{(0)}$ , and knowing that  $\cos(k_i^{(0)}h) = 0$  at  $\omega = \omega_0$ , we finally get

$$m^{(0)} \simeq \frac{D^{(0)}}{\omega_0 - \omega}, \quad (\text{A } 5)$$

with

$$D^{(0)} = 2\pi\bar{a}_i^{(0)} [J_2(\delta_i^{(0)})/\delta_i^{(0)} - J_1(\delta_i^{(0)})/k_i^{(0)2}] \quad (\text{A } 6)$$

$$= \frac{8\pi\omega_0^2 [J_2(\delta_i^{(0)})/\delta_i^{(0)} - J_1(\delta_i^{(0)})/k_i^{(0)2}]}{(\omega_0 - 2)(k_i^{(0)2} + 1)k_i^{(0)}J_1(\delta_i^{(0)})h dk_i^{(0)}/d\omega}. \quad (\text{A } 7)$$

### Appendix B. Width of the Gans' window – viscous and forcing parameters

From Meunier *et al.* (2008), Gans' solvability condition yields to the following equation for the (viscously saturated) amplitude  $A$  of a Kelvin mode forced close to

its resonance

$$(\mu + \epsilon\nu)A = if \left(1 - \frac{\epsilon A}{a_i^{(0)}}\right). \quad (\text{B } 1)$$

In (B 1), expressions of the viscous and forcing parameters  $\mu$ ,  $\nu$  and  $f$  calculated by Meunier *et al.* (2008) are

$$\mu = -\frac{\pi}{N} J_1^2(\delta_i^{(0)}) \{ \alpha_i [2h - \sin(k_i^{(0)}h)/k_i^{(0)}] + 2\beta_i \sin^2(k_i^{(0)}h) [(\delta_i^{(0)2} - 1)\omega_0^2 + 4] / (\delta_i^{(0)}\omega_0)^2 \}, \quad (\text{B } 2)$$

$$\nu = \delta_i^{(0)2} + k_i^{(0)2}, \quad (\text{B } 3)$$

and

$$f = \frac{4\pi}{N} \frac{\omega_0 + 2}{\omega_0} \sin(k_i^{(0)}h) J_1(\delta_i^{(0)}) / \delta_i^{(0)2}, \quad (\text{B } 4)$$

where

$$\alpha_i = \frac{1 + i(\delta_i^{(0)2} - 1)\omega_0^2 + 4}{\sqrt{2}(4 - \omega_0^2)\omega_0^{3/2}}, \quad (\text{B } 5)$$

$$\beta_i = \frac{1 - i}{2\sqrt{2}} \delta_i^{(0)2} \left[ \frac{1}{(2 - \omega_0)^{3/2}} + \frac{i}{(2 + \omega_0)^{3/2}} \right] \quad (\text{B } 6)$$

and

$$N = 2\pi h J_1^2(\delta_i^{(0)}) \frac{\omega_0^2(\omega_0 + 2\delta_i^{(0)2} - 2) - 4\omega_0 + 8}{\omega_0^2(4 - \omega_0^2)^2} + \frac{\pi}{k_i^{(0)}} \sin(k_i^{(0)}h) J_1^2(\delta_i^{(0)}) \frac{\omega_0^2(\omega_0 - 2\delta_i^{(0)2} - 2) - 4\omega_0 + 8}{\omega_0^2(4 - \omega_0^2)^2}. \quad (\text{B } 7)$$

From (B 1), the real part the viscously saturated amplitude can be calculated and one gets

$$\text{Re}(A) = f \frac{\epsilon f / a_i^{(0)} + \mu''}{(\epsilon f / a_i^{(0)} + \mu'')^2 + (\mu' + \epsilon\nu)^2}. \quad (\text{B } 8)$$

This quantity is supposed to become equal to the inviscid amplitude  $\epsilon a_i^{(0)}$  as  $\omega$  goes away from the resonant frequency  $\omega_0$ . Thus, from (B 8), it appears that  $A$  can be considered as equal to  $\epsilon a_i^{(0)}$  provided that the second term of the denominator is small compared to the first one. By using the Laurent's expansion (A 1) of  $a_i^{(0)}$  given in Appendix A, we finally obtain an order of magnitude for the width  $\Delta\omega$  for the Gans' window

$$\Delta\omega \sim \epsilon \bar{a}^{(0)} f^{-1} \max[|\mu|, \epsilon\nu]. \quad (\text{B } 9)$$

## Appendix C. Corrections to the inviscid wavenumbers

### C.1. Rescaled Navier–Stokes equations

Corrective flow at order 1 on the lateral wall obtained by performing viscous rescaling  $\tilde{r} = (1 - r)/\epsilon$  in the complete linear NS equation (2.1a). Equivalent rescaling for the

top wall is  $\tilde{z} = (h - z)/\epsilon$ . This couple of transformations leads to the following systems:

$$\text{lateral wall} \left\{ \begin{array}{l} -2\tilde{v}^{(0)} = \frac{\partial \tilde{p}^{(1)}}{\partial \tilde{r}}, \\ \frac{\partial \tilde{v}^{(0)}}{\partial t} - \frac{\partial^2 \tilde{v}^{(0)}}{\partial \tilde{r}^2} = 0, \\ \frac{\partial \tilde{w}^{(0)}}{\partial t} - \frac{\partial^2 \tilde{w}^{(0)}}{\partial \tilde{r}^2} = 0, \\ \frac{\partial \tilde{u}^{(1)}}{\partial \tilde{r}} = \frac{\partial \tilde{v}^{(0)}}{\partial \zeta} + \frac{\partial \tilde{w}^{(0)}}{\partial z}, \end{array} \right. \quad \text{upper wall} \left\{ \begin{array}{l} \frac{\partial \tilde{u}^{(0)}}{\partial t} - \frac{\partial^2 \tilde{u}^{(0)}}{\partial \tilde{z}^2} - 2\tilde{v}^{(0)} = 0, \\ \frac{\partial \tilde{v}^{(0)}}{\partial t} - \frac{\partial^2 \tilde{v}^{(0)}}{\partial \tilde{z}^2} + 2\tilde{u}^{(0)} = 0, \\ \frac{\partial \tilde{p}^{(1)}}{\partial z} = 0, \\ \frac{\partial \tilde{w}^{(1)}}{\partial \tilde{z}} = \frac{\partial \tilde{u}^{(0)}}{\partial r} + \frac{\tilde{u}^{(0)}}{r} + \frac{1}{r} \frac{\partial \tilde{v}^{(0)}}{\partial \zeta}. \end{array} \right. \quad (\text{C } 1a,b)$$

### C.2. Corrective flow at order 1 (boundary layer)

Normal corrective velocity  $\tilde{u}^{(0)}$  and pressure  $\tilde{p}^{(0)}$  are zero. The two tangential components of  $\tilde{\mathbf{v}}^{(0)}$ , obtained from system (C 1a), are given by

$$\tilde{v}^{(0)} = - \sum_{i=1}^{\infty} a_i^{(0)} v_i^{(0)}(1, z) e^{\kappa_i \tilde{r}} e^{i(\omega t + \varphi)}, \quad (\text{C } 2a)$$

$$\tilde{w}^{(0)} = i \left[ \sum_{i=1}^{\infty} a_i^{(0)} w_i^{(0)}(1, z) - 2 \right] e^{\kappa_i \tilde{r}} e^{i(\omega t + \varphi)}, \quad (\text{C } 2b)$$

where

$$\kappa_l = \frac{1+i}{\sqrt{2}} \sqrt{\omega}. \quad (\text{C } 3)$$

Integration of the rescaled continuity equation at order 1 provides the Ekman pumping component at the lateral wall (which is of order  $\epsilon$ )

$$u^\perp = \sum_{i=1}^{\infty} a_i^{(0)} u_i^\perp e^{i(\omega t + \varphi)}, \quad (\text{C } 4)$$

where

$$u_i^\perp = - \frac{1+i}{\sqrt{2}} \frac{1}{\omega^{3/2}(4-\omega^2)} J_1(\delta_i^{(0)}) [\omega^2(\delta_i^{(0)2} - 1) + 4] \sin(k_i^{(0)} z). \quad (\text{C } 5)$$

Corresponding expressions to (C 2) for the upper wall come from the integration of the system (C 1b). In this case

$$\tilde{u}^{(0)} = \frac{i}{2} \sum_{i=1}^{\infty} a_i^{(0)} [S_i^+(r) e^{\kappa_s \tilde{z}} + D_i^+(r) e^{\kappa_d \tilde{z}}] e^{i(\omega t + \varphi)}, \quad (\text{C } 6a)$$

$$\tilde{v}^{(0)} = \frac{1}{2} \sum_{i=1}^{\infty} a_i^{(0)} [S_i^+(r) e^{\kappa_s \tilde{z}} - D_i^+(r) e^{\kappa_d \tilde{z}}] e^{i(\omega t + \varphi)}, \quad (\text{C } 6b)$$

where

$$S_i^+(r) = u_i^{(0)}(r, h) - v_i^{(0)}(r, h), \quad D_i^+(r) = u_i^{(0)}(r, h) + v_i^{(0)}(r, h) \quad (\text{C } 7)$$

and

$$\kappa_s = -(1+i) \sqrt{\frac{2+\omega}{2}} \quad \text{and} \quad \kappa_d = -(1-i) \sqrt{\frac{2-\omega}{2}} \quad (\text{C } 8a,b)$$

Likewise, integration of the rescaled continuity equation at order 1 provides the Ekman pumping component at the upper wall

$$w^\perp = \sum_{i=1}^{\infty} a_i^{(0)} w_i^\perp e^{i(\omega t + \varphi)}, \quad (\text{C } 9)$$

with

$$w_i^\perp = -\frac{1+i}{2\sqrt{2}} \delta_i^{(0)2} J_1(\delta_i^{(0)} r) \left[ \frac{1}{(2+\omega)^{3/2}} - \frac{i}{(2-\omega)^{3/2}} \right]. \quad (\text{C } 10)$$

### C.3. Boundary condition at order $\epsilon$ on the lateral wall

The flow at order  $\epsilon$  coming from  $\epsilon$ -expansion of the wavenumbers in the inviscid flow (term in brackets in (3.2)) is supposed to compensate the Ekman pumping given by (C 4) and (C 5). Use of Kelvin's relation of dispersion enables a simplification of the derivatives of the normal velocity at  $r = 1$

$$\frac{\partial u_i^{(0)}}{\partial \delta_i} = -\frac{i}{4-\omega^2} [2J_1'(\delta_i^{(0)}) + \omega[\delta_i^{(0)} - (1/\delta_i^{(0)})] J_1(\delta_i^{(0)})] \sin(k_i^{(0)} z), \quad (\text{C } 11a)$$

$$\frac{\partial u_i^{(0)}}{\partial k_i} = 0. \quad (\text{C } 11b)$$

The condition (3.3) then leads to the expression (3.4) of  $\delta_i^{(1)}$ . Given the constitutive relation (3.6), the correction to the lengthwise wavenumber can be written

$$k_i^{(1)} = \frac{1-i}{\sqrt{2}} \sqrt{\frac{\omega}{4-\omega^2}} \delta_i^{(0)}. \quad (\text{C } 12)$$

## Appendix D. Amplitude of the additional flow

The amplitude  $a_i^{(0)}$  is determined by means of the boundary condition (3.7) at  $z = +h$ . Using the derivatives of  $w_i^{(0)}$  with respect to  $\delta_i$  and  $k_i$  at  $r = 1$ , and replacing in (3.7) each term by its expression, we obtain

$$\begin{aligned} & i \sum_i a_i^{(0)} \frac{1}{\omega} [\delta_i^{(1)} k_i^{(0)} r J_1'(\delta_i^{(0)} r) \cos(k_i^{(0)} h) + k_i^{(1)} J_1(\delta_i^{(0)} r) [\cos(k_i^{(0)} h) - k_i^{(0)} h \sin(k_i^{(0)} h)]] \\ & + i \sum_i a_i^+ \frac{k_i^{(0)} J_1(\delta_i^{(0)} r)}{\omega} \cos(k_i^{(0)} h) \\ & = + \frac{1+i}{2\sqrt{2}} \sum_i a_i^{(0)} \delta_i^{(0)2} J(\delta_i^{(0)} r) \sin(k_i^{(0)} h) \left[ \frac{1}{(2+\omega)^{3/2}} - \frac{i}{(2-\omega)^{3/2}} \right]. \end{aligned} \quad (\text{D } 1)$$

In order to derive the expression of the  $a_i^+$ , one has to express the quantity  $r J_1'(\delta_i^{(0)} r)$  as a function of the  $J_1(\delta_i^{(0)} r)$ . The Dini's expansion of  $r J_1'(\delta_i^{(0)} r)$  can be obtained by means of the formula in Watson's book (Watson 1952, pp. 580, 581), giving

$$r J_1'(\delta_i^{(0)} r) = 2 \sum_{m=1}^{\infty} \frac{\delta_m^{(0)2} S_{im}}{(\delta_m^{(0)2} - 1) [J_1(\delta_i^{(0)})]^2 + \delta_m^{(0)2} [J_1'(\delta_i^{(0)})]^2} J_1(\delta_i^{(0)} r), \quad (\text{D } 2)$$

where

$$S_{im} = \int_0^1 u^2 J_1'(\delta_m^{(0)} u) J_1(\delta_i^{(0)} u) du. \quad (\text{D } 3)$$



The integrated expression of  $S_{im}$  is as follows

$$S_{im} = \frac{1}{\delta_i^{(0)2}} J_0(\delta_i^{(0)}) J_1(\delta_i^{(0)}) - \frac{1}{2\delta_i^{(0)}} J_0^2(\delta_i^{(0)}) \quad \text{for } i = m, \quad (\text{D } 4)$$

$$\begin{aligned} S_{im} = & \frac{1}{\delta_m^{(0)}} \frac{\delta_i^{(0)} J_1(\delta_i^{(0)}) J_0(\delta_m^{(0)}) - \delta_m^{(0)} J_0(\delta_i^{(0)}) J_1(\delta_m^{(0)})}{\delta_m^{(0)2} - \delta_i^{(0)2}} \\ & \frac{1}{\delta_m^{(0)2} - \delta_i^{(0)2}} \left\{ \delta_i^{(0)} J_0(\delta_i^{(0)}) J_0(\delta_m^{(0)}) \right. \\ & + \frac{2\delta_i^{(0)}}{\delta_m^{(0)2} - \delta_i^{(0)2}} [\delta_i^{(0)} J_1(\delta_i^{(0)}) J_0(\delta_m^{(0)}) - \delta_m^{(0)} J_0(\delta_i^{(0)}) J_1(\delta_m^{(0)})] \\ & \left. + \delta_m^{(0)} J_1(\delta_i^{(0)}) J_1(\delta_m^{(0)}) \right\} \quad \text{for } i \neq m. \end{aligned} \quad (\text{D } 5)$$

A linear identification in (D 1) leads to the expression of  $a_i^+$

$$\begin{aligned} a_i^+ = & -\frac{1-i}{\sqrt{2}} \left\{ \frac{\delta_i^{(0)}}{k_i^{(0)}} a_i^{(0)} \left( \frac{\omega}{4-\omega^2} \right)^{1/2} \right. \\ & \left. + \frac{2\delta_i^{(0)2} \sum_m a_m^{(0)} k_m^{(0)} \delta_m^{(0)} \cos(k_m^{(0)} h) S_{mi}}{\omega^{1/2} k_i^{(0)} \cos(k_i^{(0)} h) [(\delta_i^{(0)2} - 1) [J_1(\delta_i^{(0)})]^2 + \delta_i^{(0)2} [J_1'(\delta_i^{(0)})]^2]} \right\} \\ & + \frac{1-i}{\sqrt{2}} a_i^{(0)} \delta_i^{(0)} \tan(k_i^{(0)} h) \left\{ \frac{(2-\omega)^{1/2}}{2(2+\omega)} + h \left[ \frac{\omega}{4-\omega^2} \right]^{1/2} \right\} \\ & - \frac{1+i}{2\sqrt{2}} a_i^{(0)} \delta_i^{(0)} \tan(k_i^{(0)} h) \frac{(2+\omega)^{1/2}}{(2-\omega)}. \end{aligned} \quad (\text{D } 6)$$

## Appendix E. Expressions of the corrective complex torques

### E.1. Expression of $\tilde{m}^{(0)}$

The viscous shear complex torque results from the integration of the shear constraint on the lateral wall, giving

$$\begin{aligned} \tilde{m}^{(0)} = & -\pi\sqrt{2\omega}(1+i) \left\{ \sum_{i=1}^{\infty} a_i^{(0)} \left[ \frac{2\delta_i^{(0)} J_1'(\delta_i^{(0)}) + \omega J_1(\delta_i^{(0)})}{4-\omega^2} \frac{\sin(k_i^{(0)} h) - k_i^{(0)} h \cos(k_i^{(0)} h)}{k_i^{(0)2}} \right. \right. \\ & \left. \left. + \frac{J_1(\delta_i^{(0)})}{\omega} \sin(k_i^{(0)} h) \right] + 2h \right\} + \pi\sqrt{2}h(1-i) \frac{1}{(2-\omega)^{1/2}} \sum_{i=1}^{\infty} a_i^{(0)} \sin(k_i^{(0)} h) J_1(\delta_i^{(0)}). \end{aligned} \quad (\text{E } 1)$$

At the resonant frequency  $\omega_0$ , coefficients of Laurent's expansion (3.10a) of  $\tilde{m}^{(0)}$  are

$$\begin{aligned} \tilde{D}_R^{(0)} = & \pi\sqrt{2} \frac{4\omega_0^2}{(\omega_0 - 2)(k_i^{(0)2} + 1)k_i^{(0)} J_1(\delta_i^{(0)}) h dk_i^{(0)}/d\omega} \left\{ \frac{h J_1(\delta_i^{(0)})}{(2-\omega_0)^{1/2}} \right. \\ & \left. - \omega_0^{1/2} \left[ \frac{2\delta_i^{(0)} J_1'(\delta_i^{(0)}) + \omega_0 J_1(\delta_i^{(0)})}{(4-\omega_0^2)k_i^{(0)2}} + \frac{J_1(\delta_i^{(0)})}{\omega_0} \right] \right\} \quad (\text{E } 2) \end{aligned}$$

$$\begin{aligned} \tilde{D}_i^{(0)} = -\pi\sqrt{2} \frac{4\omega_0^2}{(\omega_0 - 2)(k_i^{(0)2} + 1)k_i^{(0)}J_1(\delta_i^{(0)})h \, dk_i^{(0)}/d\omega} & \left\{ \frac{hJ_1(\delta_i^{(0)})}{(2 - \omega_0)^{1/2}} \right. \\ & \left. + \omega_0^{1/2} \left[ \frac{2\delta_i^{(0)}J_1'(\delta_i^{(0)}) + \omega_0J_1(\delta_i^{(0)})}{(4 - \omega_0^2)k_i^{(0)2}} + \frac{J_1(\delta_i^{(0)})}{\omega_0} \right] \right\}. \quad (\text{E } 3) \end{aligned}$$

In the previous expressions,  $\delta_i^{(0)}$ ,  $k_i^{(0)}$  and the derivative  $dk_i^{(0)}/d\omega$  are considered at  $\omega = \omega_0$ .

### E.2. Expression of $\tilde{m}^{(1)}$

Corrected pressure at order 1 in the lateral boundary layer results from the integration of the first equation of the system (C 1a).

$$\tilde{p}^{(1)} = -\frac{2}{\sqrt{\omega}} \frac{1-i}{\sqrt{2}} \sum_{i=1}^{\infty} a_i^{(0)} \frac{2\delta_i^{(0)}J_1'(\delta_i^{(0)}) + \omega J_1(\delta_i^{(0)})}{4 - \omega^2} \sin(k_i^{(0)}z) e^{\kappa z} e^{i(\omega t + \phi)}. \quad (\text{E } 4)$$

The equivalent quantity for the upper wall is zero. Integration of the previous expression leads to the complex torque  $\tilde{m}^{(1)}$

$$\begin{aligned} \tilde{m}^{(1)} = \frac{2\sqrt{2}}{\sqrt{\omega}} \pi(1+i) \sum_{i=1}^{\infty} a_i^{(0)} \frac{2\delta_i^{(0)}J_1'(\delta_i^{(0)}) + \omega J_1(\delta_i^{(0)})}{4 - \omega^2} \frac{1}{k_i^{(0)2}} & [\sin(k_i^{(0)}h) \\ & - k_i^{(0)}h \cos(k_i^{(0)}h)]. \quad (\text{E } 5) \end{aligned}$$

At the resonant frequency  $\omega_0$ , the associated coefficients in Laurent's expansion (3.10b) of  $\tilde{m}^{(1)}$  are

$$\tilde{D}_R^{(1)} = \frac{2\sqrt{2}\pi}{\sqrt{\omega_0}} \frac{4\omega_0^2}{(\omega_0 - 2)(k_i^{(0)2} + 1)k_i^{(0)}J_1(\delta_i^{(0)})h \, dk_i^{(0)}/d\omega} \frac{2\delta_i^{(0)}J_1'(\delta_i^{(0)}) + \omega_0J_1(\delta_i^{(0)})}{(4 - \omega_0^2)k_i^{(0)2}} \quad (\text{E } 6)$$

and

$$\tilde{D}_i^{(1)} = \tilde{D}_R^{(1)}. \quad (\text{E } 7)$$

In the previous expressions,  $\delta_i^{(0)}$ ,  $k_i^{(0)}$  and the derivative  $dk_i^{(0)}/d\omega$  are considered at  $\omega = \omega_0$ .

### E.3. Expression of $m^{(1)}$

$$\begin{aligned} m^{(1)} = -\pi\sqrt{2} \sum_{i=1}^{\infty} [(d_i - e_i + c_i) & \\ & + i(d_i + e_i + c_i)] \left[ \frac{J_1(\delta_i^{(0)})}{k_i^{(0)2}} [\sin(k_i^{(0)}h) - k_i^{(0)}h \cos(k_i^{(0)}h)] - \frac{J_2}{\delta_i^{(0)}} \sin(k_i^{(0)}h) \right] \\ & + \pi\sqrt{2}(1+i) \left( \frac{\omega}{4 - \omega^2} \right)^{1/2} \sum_{i=1}^{\infty} a_i^{(0)} \delta_i^{(0)} \left[ \frac{J_2(\delta_i^{(0)})}{\delta_i^{(0)}} h \cos(k_i^{(0)}h) \right. \\ & \left. - \frac{J_1}{k_i^{(0)3}} [k_i^{(0)2}h^2 \sin(k_i^{(0)}h) - 2 \sin(k_i^{(0)}h) + 2k_i^{(0)}h \cos(k_i^{(0)}h)] \right] \\ & - \pi\sqrt{2}(1+i)\omega^{-1/2} \sum_{i=1}^{\infty} a_i^{(0)} \delta_i^{(0)} \left[ \frac{J_1'(\delta_i^{(0)})}{k_i^{(0)2}} [\sin(k_i^{(0)}h) - k_i^{(0)}h \cos(k_i^{(0)}h)] \right. \\ & \left. - \sin(k_i^{(0)}h) \left[ \frac{J_1(\delta_i^{(0)})}{\delta_i^{(0)}} - 3 \frac{J_2(\delta_i^{(0)})}{\delta_i^{(0)2}} \right] \right] \quad (\text{E } 8) \end{aligned}$$

with

$$c_i = -\frac{2\delta_i^{(0)2} \sum_m a_m^{(0)} k_m^{(0)} \delta_m^{(0)} \cos(k_m^{(0)} h) S_{mi}}{\omega^{1/2} k_i^{(0)} \cos(k_i^{(0)} h) [(\delta_i^{(0)2} - 1) [J_1(\delta_i^{(0)})]^2 + \delta_i^{(0)2} [J_1'(\delta_i^{(0)})]^2]} - a_i^{(0)} \frac{\delta_i^{(0)}}{k_i^{(0)}} \left(\frac{\omega}{4 - \omega^2}\right)^{1/2}, \quad (\text{E } 9)$$

$$d_i = a_i^{(0)} \delta_i^{(0)} \tan(k_i^{(0)} h) \left[ \frac{1}{2} \frac{(2 - \omega)^{1/2}}{(2 + \omega)} + h \left(\frac{\omega}{4 - \omega^2}\right)^{1/2} \right] \quad (\text{E } 10)$$

$$\text{and } e_i = a_i^{(0)} \delta_i^{(0)} \tan(k_i^{(0)} h) \frac{1}{2} \frac{(2 + \omega)^{1/2}}{(2 - \omega)}. \quad (\text{E } 11)$$

The coefficients of poles of order 2 in Laurent's expansion (3.11) of  $m^{(1)}$  are given by

$$C_R^{(1)} = \sqrt{2\pi} \frac{4\omega_0^2 \delta_i^{(0)}}{(\omega_0 - 2)(k_i^{(0)2} + 1) k_i^{(0)} J_1(\delta_i^{(0)}) (h \, dk_i^{(0)}/d\omega)^2} \left[ \frac{J_2(\delta_i^{(0)})}{\delta_i^{(0)}} - \frac{J_1(\delta_i^{(0)})}{k_i^{(0)2}} \right] \\ \times \left[ h \left(\frac{\omega_0}{4 - \omega_0^2}\right)^{1/2} + \frac{1}{2} \frac{(1 - \omega_0)^{1/2}}{2 + \omega_0} - \frac{1}{2} \frac{(1 + \omega_0)^{1/2}}{2 - \omega_0} \right], \quad (\text{E } 12)$$

$$C_I^{(1)} = \sqrt{2\pi} \frac{4\omega_0^2 \delta_i^{(0)}}{(\omega_0 - 2)(k_i^{(0)2} + 1) k_i^{(0)} J_1(\delta_i^{(0)}) (h \, dk_i^{(0)}/d\omega)^2} \left[ \frac{J_2(\delta_i^{(0)})}{\delta_i^{(0)}} - \frac{J_1(\delta_i^{(0)})}{k_i^{(0)2}} \right] \\ \times \left[ h \left(\frac{\omega_0}{4 - \omega_0^2}\right)^{1/2} + \frac{1}{2} \frac{(1 - \omega_0)^{1/2}}{2 + \omega_0} + \frac{1}{2} \frac{(1 + \omega_0)^{1/2}}{2 - \omega_0} \right]. \quad (\text{E } 13)$$

As usually  $\delta_i^{(0)}$ ,  $k_i^{(0)}$  and the derivative  $dk_i^{(0)}/d\omega$  are considered at the resonant frequency  $\omega = \omega_0$ . The coefficients  $D_R^{(1)}$  and  $D_I^{(1)}$  of the pole of order 1 in  $m^{(1)}$  Laurent's expansion are not given as their expressions are too lengthy. They can be easily obtained by using a formal calculation software.

#### REFERENCES

- D'AMICO, W. P. 1977 Inertial mode corrections for the large amplitude motion of a liquid-filled gyroscope. PhD Thesis, University of Delaware, Newark.
- D'AMICO, W. P. & ROGERS, T. H. 1981 Yaw instabilities produced by rapidly rotating, highly viscous liquids. *AIAA paper 81-0224*.
- FORTIN, M. & GLOWINSKI, R. 1982 *Méthodes de Lagrangien augmenté. Application à la résolution numérique de problèmes aux limites*. Paris, Dunod.
- FULTZ, D. 1959 A note on overstability and elastoid-inertia oscillations of Kelvin, Solberg and Bjerknes. *J. Meteorol.* **16**, 199–208.
- GANS, R. F. 1970 On the precession of a resonant cylinder. *J. Fluid Mech.* **476**, 865–872.
- GANS, R. F. 1984 Dynamics of a near-resonant fluid-filled gyroscope. *AIAA J.* **22**, 1465–1471.
- GARG, S. C., FURUNOTO, N. & VANYO, J. P. 1986 Spacecraft nutational instability prediction by energy dissipation measurements. *J. Guid.* **9** (3), 357–361.
- GREENHILL, A. G. 1880 On the general motion of a liquid ellipsoid. *Proc. Camb. Phil. Soc.* **4** (4).
- GREENSPAN, H. P. 1968 *The Theory of Rotating Fluids*. Cambridge University Press.
- HARLOW, F. H & WELSH, J. E. 1965 Numerical calculation of time dependant viscous incompressible flows. *Phys. Fluids* **8**, 2182–2189.
- KARPOV, B. G. 1962 Experimental observations of the dynamic behaviour of liquid-filled shell. *Tech. Rep. BRL Report 1171*. Aberdeen Proving Ground, MD.

- KARPOV, B. G. 1965 The effect of Reynolds number on resonance. *Tech. Rep.* BRL Report 1302. Aberdeen Proving Ground, MD.
- KERSWELL, R. R. 1999 Secondary instabilities in rapidly rotating fluids: inertial wave breakdown. *J. Fluid Mech.* **382**, 283–306.
- KERSWELL, R. R. & BARENGHI, C. F. 1995 On the viscous decay rates of inertial waves in a rotating circular cylinder. *J. Fluid Mech.* **285**, 203–214.
- KOBINE, J. J. 1995 Inertial wave dynamics in a rotating and precessing cylinder. *J. Fluid Mech.* **303**, 233–352.
- KOBINE, J. J. 1996 Azimuthal flow associated with inertial wave resonance in a precessing cylinder. *J. Fluid Mech.* **319**, 387–406.
- KUDLICK, M. 1966 On the transient motions in a contained rotating fluid. PhD thesis, Massachusetts Institute of Technology, Cambridge, MA.
- LAGRANGE, R., MEUNIER, P., ELOY, C. & NADAL, F. 2008 Instability of a fluid inside a precessing cylinder. *Phys. Fluids* **20**, 081701.
- MAHALOV, A. 1993 The instability of rotating fluid columns subjected to a weak external Coriolis force. *Phys. Fluids A* **5** (4), 891–900.
- MANASSEH, R. 1992 Breakdown regimes of inertia waves in precessing cylinder. *J. Fluid Mech.* **243**, 261–296.
- MANASSEH, R. 1994 Distortions of inertia waves in a rotating fluid cylinder forced near its fundamental mode resonance. *J. Fluid Mech.* **265**, 345–370.
- MANASSEH, R. 1996 Nonlinear behaviour of contained inertia waves. *J. Fluid Mech.* **315**, 151–173.
- MCEWAN, A. D. 1970 Inertial oscillations in a rotating fluid cylinder. *J. Fluid Mech.* **40**, 603–640.
- MEUNIER, P., ELOY, C., LAGRANGE, R. & NADAL, F. 2008 Rotating fluid cylinder subject to weak precession. *J. Fluid Mech.* **599**, 405–440.
- MILNE, E. A. 1940 On the stability of a liquid-filled shell (U). EBD report No. 6.
- MURPHY, C. H. 1982 Angular motion of a spinning projectile with a viscous payload. *Tech. Rep.* ARBRL-TR-02422. US Army Ballistic Research Laboratory, Aberdeen Proving Ground, MD.
- SCOTT, W. E. & D'AMICO, W. P. 1973 Amplitude-dependent behavior of a liquid-filled gyroscope. *J. Fluid Mech.* **60**, 751–758.
- STEWARTSON, K. 1958 On the stability of a spinning top containing liquid. *J. Fluid Mech.* **5**, 577–592.
- THOMSON, W. SIR 1880 Vibrations of a columnar vortex. *Phil. Mag.* **10**, 155–168.
- THOMSON, R. 1970 Diurnal tides and shear instabilities in a rotating cylinder. *J. Fluid Mech.* **40**, 737–751.
- VANYO, J. P. 1993 *Rotating Fluids in Engineering and Science*. Dover.
- VINCENT, S. & CALTAGIRONE J.-P. 2000 A one-cell local multigrid method for solving unsteady incompressible multiphase flow. *J. Comput. Phys.* **163**, 172–215.
- VAN DER VORST, H. A. 1992 Bi-CGSTAB: a fast and smoothly converging variant of Bi-CG for the solution of nonsymmetric linear system. *SIAM J. Sci. Stat. Comput.* **13**, 631–644.
- WALEFFE, F. 1989 The three-dimensional instability of a strained vortex and its relation to turbulence. PhD thesis, Massachusetts Institute of Technology, Cambridge, MA.
- WARD, G. N. 1959 Appendix to K. Stewartson “On the stability of a spinning top containing liquid”. *J. Fluid Mech.* **5**, 577–592.
- WATSON, G. N. 1952 *Theory of Bessel Functions*. Cambridge University Press.
- WEDEMEYER, E. H. 1965 Dynamics of a liquid-filled shell: theory of viscous corrections to Stewartson’s stability problem. BRL Report N 1287. US Army Ballistic Research Laboratory, Aberdeen Proving Ground, MD.
- WEDEMEYER, E. H. 1966 Viscous corrections to Stewartson’s stability criterion. BRL Report N 1325. US Army Ballistic Research Laboratory, Aberdeen Proving Ground, MD.
- WHITING, R. D. & GERBER, N. 1981 Dynamics of a liquid-filled gyroscope: update of theory and experiment. *Tech. Rep.* ARBRL-TR-02221. US Army Ballistic Research Laboratory, Aberdeen Proving Ground, MD.